ARTICLE

Interleukin-17–induced neutrophil extracellular traps mediate resistance to checkpoint blockade in pancreatic cancer

Yu Zhang[1]*, Vidhi Chandra[1]* , Erick Riquelme Sanchez[1,2]* , Prasanta Dutta[3], Pompeyo R. Quesada[1] , Amanda Rakoski[1] , Michelle Zoltan[1] , Nivedita Arora[4] , Seyda Baydogan[1] , William Horne[5], Jared Burks[6] , Hanwen Xu[1] , Perwez Hussain[7], Huamin Wang[8,9] , Sonal Gupta[8] , Anirban Maitra[8,9,10] , Jennifer M. Bailey[11] , Seyed J. Moghaddam[12] , Sulagna Banerjee[13] , Ismet Sahin[14] , Pratip Bhattacharya[3], and Florencia McAllister[1,15]

Pancreatic ductal adenocarcinoma (PDAC) remains a lethal malignancy with an immunosuppressive microenvironment that is resistant to most therapies. IL17 is involved in pancreatic tumorigenesis, but its role in invasive PDAC is undetermined. We hypothesized that IL17 triggers and sustains PDAC immunosuppression. We inhibited IL17/IL17RA signaling using pharmacological and genetic strategies alongside mass cytometry and multiplex immunofluorescence techniques. We uncovered that IL17 recruits neutrophils, triggers neutrophil extracellular traps (NETs), and excludes cytotoxic CD8 T cells from tumors. Additionally, IL17 blockade increases immune checkpoint blockade (PD-1, CTLA4) sensitivity. Inhibition of neutrophils or Padi4-dependent NETosis phenocopies IL17 neutralization. NMR spectroscopy revealed changes in tumor lactate as a potential early biomarker for IL17/PD-1 combination efficacy. Higher expression of IL17 and PADI4 in human PDAC corresponds with poorer prognosis, and the serum of patients with PDAC has higher potential for NETosis. Clinical studies with IL17 and checkpoint blockade represent a novel combinatorial therapy with potential efficacy for this lethal disease.

Introduction

Pancreatic ductal adenocarcinoma (PDAC) remains one of the deadliest malignancies, with limited treatment options. Several immunotherapy approaches have emerged in the past decade, and immune checkpoint blockade has been approved for use in several cancer types (Le et al., 2015; Brahmer et al., 2015; Diaz and Le, 2015; Wolchok et al., 2017; D'Angelo et al., 2017; Long et al., 2017). Unfortunately, immune checkpoint inhibitors have not proved efficacious in treating pancreatic cancer (Royal et al., 2010; Brahmer et al., 2012; Herbst et al., 2014; Patnaik et al., 2015; Balachandran et al., 2019). Recently, considerable interest has been focused on combining checkpoint inhibitors with other immunotherapies, antibodies, or vaccines to target or prime the tumor microenvironment, one of the main drivers of the immunosuppression that prevails in pancreatic cancer (Lutz et al., 2014; Highfill et al., 2014; Zhu et al., 2014; Winograd et al., 2015).

Several cell types have been implicated in contributing to the immunosuppressive microenvironment that supports PDAC growth: macrophages, myeloid-derived suppressor cells (MDSC), fibroblasts, and T regulatory cells (Clark et al., 2007; Bayne et al., 2012). Strategies that target these cell types in combination with immune checkpoint inhibitors have been proved to have synergistic antitumoral effects in preclinical models of pancreatic cancer as well as other cancer types (Zhang et al., 2017; Zhu et al., 2014; Highfill et al., 2014; Feig et al., 2013; Provenzano et al., 2012), and some of them are being tested in ongoing clinical trials (NCT02452424, NCT02777710).

....

[1]Department of Clinical Cancer Prevention, The University of Texas MD Anderson Cancer Center, Houston, TX;   [2]Center for Integrative Biology, Faculty of Science, Universidad Mayor, Santiago, Chile;   [3]Cancer Systems Imaging, The University of Texas MD Anderson Cancer Center, Houston, TX;   [4]University of Minnesota, Minneapolis, MN;   [5]Richard King Mellon Foundation Institute for Pediatric Research, Children's Hospital of Pittsburgh, Pittsburgh, PA;   [6]Department of Leukemia, The University of Texas MD Anderson Cancer Center, Houston, TX;   [7]Laboratory of Human Carcinogenesis, National Cancer Institute, Bethesda, MD;   [8]Department of Anatomical Pathology, The University of Texas MD Anderson Cancer Center, Houston, TX;   [9]Department of Translational Molecular Pathology, The University of Texas MD Anderson Cancer Center, Houston, TX;   [10]Sheikh Ahmed Center for Pancreatic Cancer Research, The University of Texas MD Anderson Cancer Center, Houston, TX;   [11]Department of Gastroenterology, University of Texas Health Sciences Center, Houston, TX;   [12]Pulmonary Medicine, The University of Texas MD Anderson Cancer Center, Houston, TX; [13]Department of Surgery, Sylvester Comprehensive Cancer Center, University of Miami Health System, Miami, FL;   [14]Department of Engineering, Texas Southern University, Houston, TX;   [15]Gastrointestinal Medical Oncology, The University of Texas MD Anderson Cancer Center, Houston, TX.

*Y. Zhang, V. Chandra, and E. Riquelme Sanchez contributed equally to this work;   Correspondence to Florencia McAllister: fmcallister@mdanderson.org.
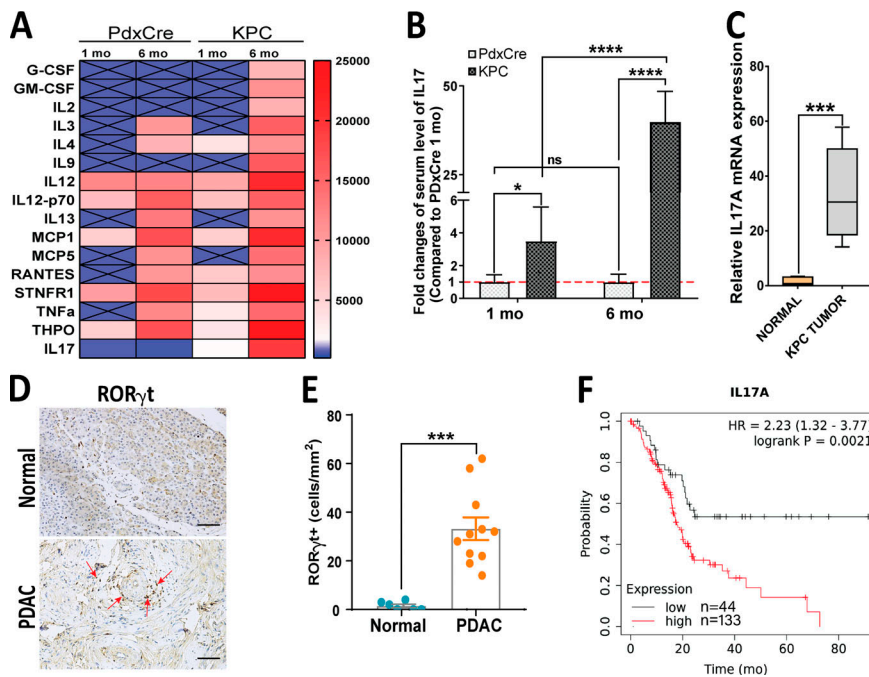
Figure 1. **IL17-secreting cells are increased in murine and human pancreatic adenocarcinoma carcinoma. (A)** Heat map representing serum levels of cytokines from a spontaneous pancreatic adenocarcinoma mouse model (KPC) and control mice (Pdx1-Cre) at 1 mo and 6 mo of age. **(B)** Serum IL17 levels measured by Luminex assay in Pdx-Cre and KPC mice at 1 mo and 6 mo of age. Results show the mean ± SD of fold changes from KPC over Pdx-Cre (n = 5). **(C)** Relative IL17 mRNA expression measured by quantitative RT-PCR in normal pancreatic tissue and tumor tissue formed from KPC cells orthotopically implanted into syngeneic mice. Results show the mean ± SD of fold changes from KPC tumors over normal pancreas (n = 5). **(D)** Th17 cells in normal human pancreatic tissue and PDAC based on RORγt staining by IHC. Scale bars represent 50 µm. **(E)** Quantification of human RORγt^{+} cells on tissue from normal versus PDAC. **(F)** Kaplan-Meier survival curves comparing survival of patients with PDAC with low versus high levels of median IL17A expression. *, P < 0.05; ***, P < 0.001; ****, P < 0.0001.

We have previously described that IL17, a cytokine secreted mostly by CD4^{+} and γδ T cells during pancreatic tumorigenesis, is involved in the initiation and development of pancreatic precursor lesions of PDAC (McAllister et al., 2014). The interaction between IL17 and IL17RA, which is overexpressed in the epithelium upon Kras activation, promotes a stemness signature in premalignant lesions (McAllister and Leach, 2014; Zhang et al., 2018). In the present study, we detected high levels of IL17 in tumors from both autochthonous and transplanted orthotopic PDAC mouse models. We found that IL17 sustains immunosuppression by decreasing CD8^{+} T cell recruitment and activation while promoting neutrophil recruitment in the tumor microenvironment. IL17 blockade sensitizes tumors to checkpoint inhibitors in a CD8^{+} T cell–dependent manner. We explored mechanisms implicated in this process as well as biomarkers.
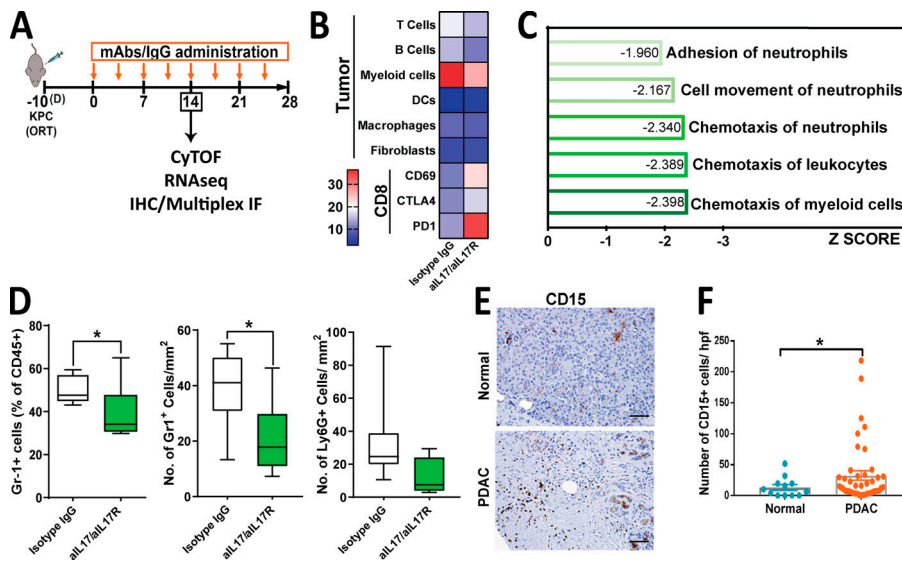
Results

IL17-secreting cells are increased in murine and human pancreatic adenocarcinoma

Given the key role that IL17 exerts in the initiation and progression of pancreatic premalignant lesions (McAllister et al., 2014), we first aimed to determine the dynamic systemic levels of IL17 that change with progression in pancreatic adenocarcinoma mouse models. To this end, we measured the serum concentration of a panel of cytokines in the autochthonous K-ras[LSL.G12D/+];p53[R172H/+];PdxCre (KPC) pancreatic adenocarcinoma mouse model at two time points (1 and 6 mo). We found that serum levels of several cytokines were increased in KPC mice in an age-dependent manner (Fig. 1 A). When we compared KPC mice with age-matched control PdxCre mice, we found that serum levels of IL17 drastically increased with PDAC progression (Fig. 1, A and B). We then measured IL17 in an orthotopic PDAC

mouse model in which KPC cells were allografted into the pancreas of syngeneic animals and found that IL17 mRNA expression in orthotopic pancreatic tumors was significantly upregulated compared with normal pancreas (Fig. 1 C). We also detected T helper type 17 (Th17) cells in human PDAC tissue, which are absent or in very low numbers in normal tissue (Fig. 1, D and E). We also found that patients with higher IL17A expression in their pancreatic tumors, based on The Cancer Genome Atlas (TCGA), had significantly worse prognosis than those with lower IL17 expression (hazard ratio [HR], 2.2; P = 0.0021; Fig. 1 F).

IL17 induces recruitment of neutrophils to pancreatic tumors

To understand if IL17 plays a role in modulating the composition of the PDAC tumor microenvironment, we blocked IL17 signaling using anti-IL17/anti-IL17R neutralizing antibodies or IgG isotype control as previously described (McAllister et al., 2014) in an orthotopic pancreatic cancer mouse model, and, after 14 d from treatment initiation, we performed immunoprofiling using several methodologies (Fig. 2 A). To first distinguish which cell types within the pancreatic tumor microenvironment were modulated by IL17, we performed mass cytometry (CyTOF) analysis on tumors from mice treated with anti-IL17/IL17RA mAb versus isotype. This assay revealed that IL17 neutralization decreases myeloid cell recruitment, already known to be modulated by IL17 during pancreatic premalignancy stages (McAllister et al., 2014), whereas it upregulates CD69 and PD-1 expression on CD8^{+} T cells, markers of activation and exhaustion, respectively (Fig. 2 B). To determine genes and pathways modulated by IL17 we performed RNA sequencing of the tumors and, using Ingenuity Pathway Analysis, we found that chemotaxis of myeloid cells, leukocytes, and neutrophils, along with cell movement and adhesion of neutrophils, were predicted to be the most significant cellular functions represented

Zhang et al.
IL17-induced NETs and immunosuppression in PDAC

Journal of Experimental Medicine   2 of 14
https://doi.org/10.1084/jem.20190354

Figure 2. **IL17 recruits neutrophils to the pancreatic tumor microenvironment. (A)** Experimental protocol for orthotopic implantation of KPC cells into syngeneic WT mice followed by treatment with anti-IL17 and anti-IL17R mAb (aIL17/aIL17R) versus control isotype IgG. CyTOF, RNA sequencing (RNAseq), IHC, and multiplex IF were performed at 14 d after treatment initiation. **(B)** Heat map showing distribution of tumor-infiltrating immune cells as identified by CyTOF analysis of tumors from A, represented as a percentage of total CD45+ cells (n = 5/group). DC, dendritic cell. **(C)** Ingenuity Pathway Analysis showing the top five cellular functions predicted using genes significantly downregulated in tumors from A. As indicated on the x axis, biological functions with P < 0.05 are sorted based on Z scores. **(D)** Quantification of Gr1+ cells measured in tumors from A by flow cytometry (left panel) or IHC (middle panel) and Ly6G+ cells measured by IHC (right panel). Results are expressed as the relative percentage of total gated CD45+ cells for flow cytometry and total number of cells/mm² for IHC. **(E)** Representative images of neutrophils infiltrating human PDAC tissue versus normal adjacent tissue by CD15 staining performed by IHC. Scale bars represent 50 μm. **(F)** Quantification of CD15 staining in E. Results are expressed as the number of CD15+ cells per high-power field (hpf). *, P < 0.05.

by the genes upregulated by IL17 (Table S1 and Fig. 2 C) and may contribute to the generation and maintenance of the immunosuppressive microenvironment that characterizes pancreatic adenocarcinoma. We then used flow cytometry and immunohistochemistry (IHC) to closely examine neutrophils using both Gr1 and Ly6G antibodies, and, through both assays, we validated that IL17 decreased neutrophil infiltration at 4 wk in orthotopic (Fig. 2 D) and subcutaneous models (Fig. S1, A and B), whereas immunosuppressive cellular populations in the spleen were unaltered (Fig. S1 C), suggesting a local effect in the tumor microenvironment rather than a systemic effect. We then evaluated for human relevance and found that CD15+ cells, human neutrophils, were significantly increased in PDAC compared with normal tissue (Fig. 2, E and F). Subsequently, we analyzed data derived from RNA sequencing of KPC cells exposed to IL17 in vitro, as previously described (McAllister et al., 2014), and found that the expression levels of several cytokines and chemokines capable of recruiting neutrophils were significantly induced after IL17 treatment, including Cxcl5, Cxcl3, Csf3, Ccl20, and Cxcl1 (Fig. S1 D). Previous reports have attributed immunosuppressive activity to CXCR2-dependent neutrophil recruitment to the PDAC tumor microenvironment (Nywening et al., 2018; Chao et al., 2016). IL17 signaling is upstream from these chemotactic molecules associated with neutrophil chemotaxis, and therefore it is expected that its inhibition would result in broader efficacy. Given these results, we focused on gaining a deep understanding of the effects of IL17 mediated by neutrophil recruitment and function.
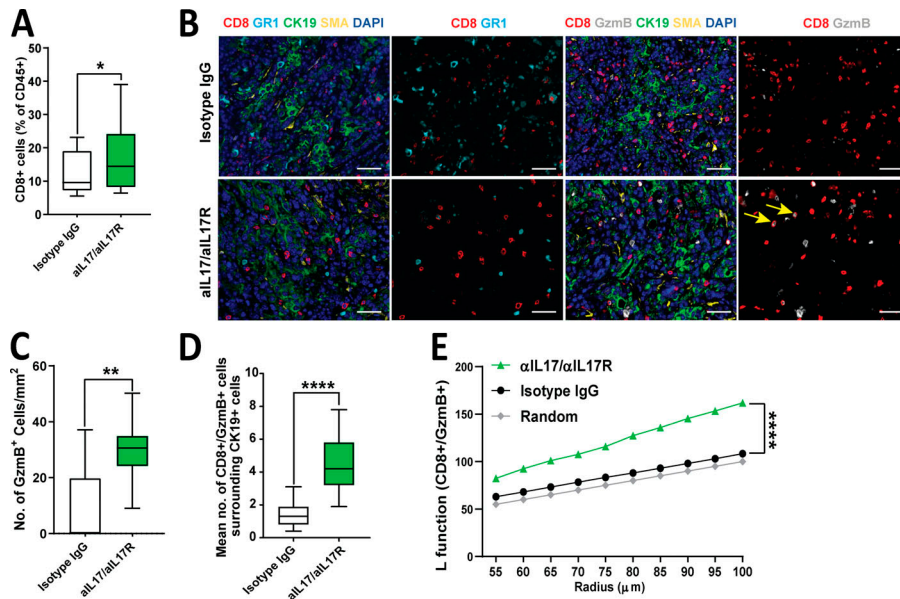
IL17 signaling favors tumor CD8+ T cell inactivation and spatial exclusion

Tumoral immune cell analysis by flow cytometry revealed that IL17 blockade mildly increased the total number of CD8+ T cells (Fig. 3 A). We then asked if IL17 blockade may also alter the spatial distribution of immune cells within the tumors. To achieve this, we performed immune profiling by opal multiplex immunofluorescence (IF), which allowed simultaneous detection of several immune cells in the tumor (Fig. 3 B and Fig. S2 A). We found that the number of activated CD8+ T cells (measured by CD8+Gzmb+) was significantly increased in tumors (Fig. 3, B and C) and were in closer proximity to tumor cells (CK19+) upon IL17 blockade (Fig. 3, B and D; and Fig. S2 B). This indicated that IL17 neutralization not only increased CD8+ T cell activation but also allowed spatial redistribution favoring their proximal migration to tumor cells. Furthermore, we performed deeper automated spatial quantification using algorithms (L function) that allowed us to determine if spatial distribution of CD8+ T cells is random, dispersed, or clustered around tumors. Using this methodology, we found that CD8+ T cells are randomly dispersed in tumors treated with isotype IgG, whereas clustering around tumors is favored upon IL17 neutralization (Fig. 3 E). Taken together, IL17/IL17R signaling induces remodeling of the pancreatic tumor microenvironment, favoring tumor exclusion and inactivation of CD8+ T cells.

Pharmacological and genetic blockade of IL17 signaling overcomes resistance to immune checkpoint inhibition

Because IL17 blockade modulates the tumor microenvironment favoring CD8+ T cell activation, we hypothesized that it may elicit antitumor responses against pancreatic cancer. To test this, we first used a subcutaneous syngeneic mouse model in which KPC tumor-bearing mice were treated with IgG isotype control versus anti-IL17/IL17R mAb (Fig. S1 A). We found that despite the strongly favorable microenvironment modulation induced by IL17 blockade, tumor growth was not affected compared with isotype-treated mice (Fig. 4 A). We hypothesized that this resistance could be mediated by modulation of immune checkpoint molecules in the setting of persistent immune activation. We measured immune checkpoint molecules and exhaustion

Zhang et al.
IL17-induced NETs and immunosuppression in PDAC

Journal of Experimental Medicine   3 of 14
https://doi.org/10.1084/jem.20190354

Figure 3. **IL17 signaling modulates the pancreatic tumor microenvironment. (A)** Quantification of CD8+ cells by flow cytometry measured in tumors from Fig. 2 A treated with isotype IgG or aIL17/aIL17R antibodies. Results are expressed as the relative percentage of total gated CD45+ cells. **(B)** Representative pictures of multiplex IF staining showing CD8, Gr1, GzmB, CK19, SMA, and DAPI staining in tumor tissues from Fig. 2 A. Scale bars represent 50 μm. Yellow arrows indicate double-positive cells for CD8 and GzmB staining. **(C)** Quantification of Gzmb+ cells measured in tumors shown in B by multiplex IF. Results are expressed as the total number of cells/mm². **(D)** Spatial quantification of CD8+Gzmb+ cells surrounding CK19+ cells (within 40 μm) measured in tumors shown in B by multiplex IF. **(E)** Clustering of CD8+GzmB+ cells surrounding CK19+ cells represented as an L function measured in tumors in B. Random dispersion is denoted by the gray line. *, P < 0.05; **, P < 0.01; ****, P < 0.0001.

marker expression and discovered that the PD-L1 mRNA expression in whole tumors increased in response to IL17 signaling inhibition, whereas the exhaustion markers Eomes and CD44 remained unchanged (Fig. S1, E and F).

Based on these results, we hypothesized that pharmacological blockade of both IL17 and PD-L1/PD-1 signaling would achieve synergistic antitumoral efficacy against pancreatic adenocarcinoma. To this end, we randomized subcutaneous KPC allograft-bearing mice into four groups that received the following treatments: (1) IgG isotype control antibodies, (2) dual anti-IL17/IL17R mAb (rat antimouse; Amgen), (3) anti–PD-1 mAb (rat antimouse; Bio X Cell), and (4) triple combination of anti-IL17/IL17R and anti–PD-1 antibodies.

We found that anti-IL17/IL17R or anti–PD-1 antibodies did not have antitumoral efficacy alone, and only the triple combination of anti-IL17/IL17R/PD-1 antibodies had a significant synergistic effect in decreasing tumor growth in subcutaneous PDAC models (Fig. 4 A and Fig. S1 G). Adapting RECIST criteria (Response Evaluation Criteria in Solid Tumors; Eisenhauer et al., 2009) to assess murine response to the treatment, we found that 5 of 9 mice exhibited responses to triple-combination treatment, whereas only 1 of 10 mice showed a response to anti–PD-1 treatment and none of the treated mice had responses to anti-IL17 or isotype control treatment (Fig. S1 H).

We then performed a second experiment with the same treatment arms using a murine PDAC orthotopic tumor model
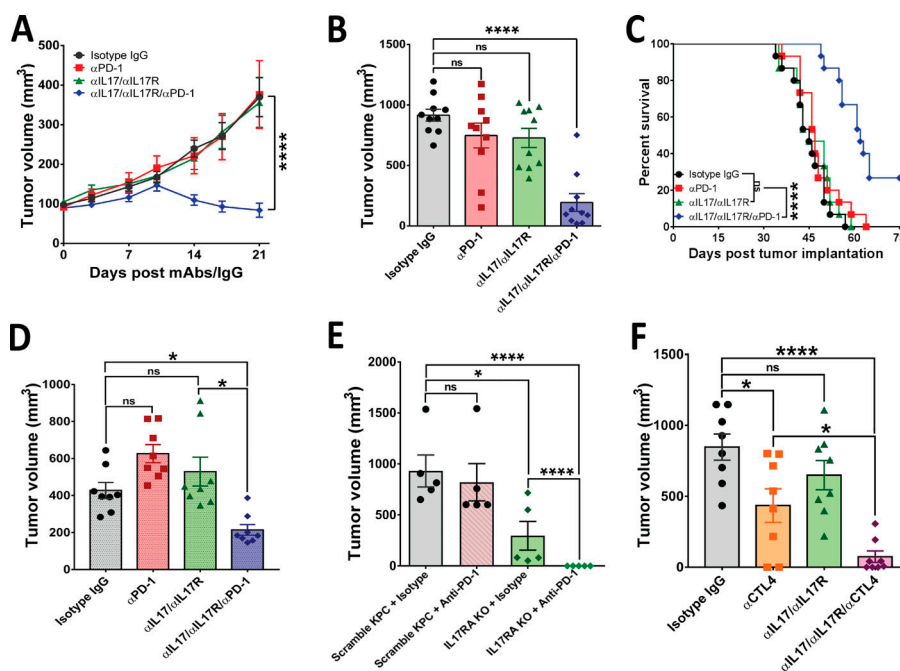
Figure 4. **Pharmacological and genetic blockade of IL17 signaling overcomes resistance to immune checkpoint inhibition. (A)** Tumor growth curves for subcutaneously implanted KPC cells treated with anti-IL17/IL17R/PD-1 antibodies as described in Fig. S1 A (n = 10 mice/group). **(B)** Tumor volumes of orthotopically implanted KPC cells treated with anti-IL17/IL17R/PD-1 antibodies as described in Fig. 2 A (n = 10 mice/group). **(C)** Kaplan-Meier curves for syngeneic mice orthotopically implanted with KPC cells and treated with the indicated antibodies as described in Fig. 2 A (n = 10 mice/group). **(D)** Tumor volumes of orthotopically implanted mT3 cells treated with anti-IL17/IL17R/PD-1 antibodies as described in Fig. 2 A (n = 8 mice/group). **(E)** Tumor volumes of orthotopically implanted KPC cells (with genetic deletion of IL17R by CRISPR/Cas9 versus scramble control) into syngeneic mice in presence/absence of aPD-1 (n = 5 mice/group). **(F)** Tumor volumes of orthotopically implanted KPC cells into syngeneic mice treated with anti-IL17/CTLA4 antibodies as described in Fig. 2 A (n = 7 mice/group). *, P < 0.05; ****, P < 0.0001.

Zhang et al.
IL17-induced NETs and immunosuppression in PDAC

Journal of Experimental Medicine   4 of 14
https://doi.org/10.1084/jem.20190354

because it more closely mimics the PDAC tumor microenvironment (Fig. 2 A). We started treatment 10 d after implantation, when all tumors had a similar size based on magnetic resonance imaging (MRI) assessments (Fig. S3, A and B).

After 4 wk of treatment, we also detected a significant reduction in tumor size following combination IL17/IL17RA and PD-1 inhibition compared with the IgG control or single-treatment arms (Fig. 4 B). The response rate for triple-combination treatment was 50%, whereas no responders were found in the control or single-treatment arms (Fig. S3 C). A survival experiment was performed with the same four arms using the murine orthotopic model, and a significant extension in mean survival was observed in mice treated with the triple combination of IL17/IL17R and PD-1 blockade (62 d) compared with mice treated with IgG control (45 d), single-agent anti–PD-1 (47 d), or dual anti-IL17/IL17R antibodies (45 d; Fig. 4 C). Of note, 4 of 15 mice from the triple-combination group survived by day 75, when the experiment ended.

We then aimed to tease apart the individual contribution of each anti-IL17 and anti-IL17R antibody when added to anti–PD-1. We used mAb against IL17E (rat antimouse; Amgen), another ligand of IL17RA, and found that its neutralization does not increase sensitivity to PD-1 blockade. Moreover, we observed that individual neutralization of IL17A or IL17RA significantly increased sensitivity to PD-1 blockade, but with less efficacy than their combination (Fig. S3 D). Based on these results, we continued using the combination of IL17A/IL17RA antibodies for the rest of the study.

We compared the histopathology, proliferation index (Ki67), and apoptosis level (cleaved caspase 3) between the groups and did not find any major differences (Fig. S3 E). To check if the observed antitumoral effect was consistent with other PDAC cell lines, we used mT3 cells, which are derived from murine organoids generated from KPC mouse PDAC lesions (Boj et al., 2015). Interestingly, single treatment with anti–PD-1 resulted in larger tumors with these cells, which may be either a temporary effect or due to resistance patterns of these organoid-based tumors. Nevertheless, we found a similar synergistic effect of treatment with anti-IL17/IL17R/PD-1 using these cells (Fig. 4 D).

We then hypothesized that IL17 primarily signals through pancreatic cancer cells, which secrete chemotactic factors that direct neutrophil recruitment, ultimately inducing and maintaining tumor immunosuppression. We used a genetic strategy to specifically knock out IL17R from KPC cells using CRISPR/Cas9 gene editing (Fig. S3 F) and performed orthotopic implantation of these cells versus scrambled control cells with intact IL17R. When we performed imaging at day 10 after implantation, one-third of mice did not meet inclusion criteria for the study because they had no tumors or had tumors smaller than 100 mm³, likely due to early function of IL17 on tumor initiation (Zhang et al., 2018), and those mice were excluded from randomization. When we sacrificed mice, we found that pancreatic tumors formed with IL17R-KO KPC cells were significantly smaller than those formed with IL17R intact scramble-treated cells, and complete tumor remission was observed when mice implanted with IL17R-KO KPC cells were treated with anti–PD-1 antibodies (Fig. 4 E). These data strongly

suggest that the epithelial IL17/IL17RA signaling is mediating the immunosuppressive effect during pancreatic cancer.

Finally, to determine if IL17 blockade sensitizes tumors selectively to PD-1 only or to other checkpoint inhibitors as well, we treated mice with a combination of IL17/IL17R inhibitors and anti-CTLA4 mAb (rat antimouse; Bio X Cell). We found that IL17/IL17R blockade significantly increased sensitivity to CTLA4 inhibition as well (Fig. 4 F), suggesting that IL17 inhibition sensitizes tumors to checkpoint blockade nonspecifically. To summarize, through a comprehensive combination of pharmacological and genetic approaches, we confirmed the critical role of the IL17–IL17R axis in controlling tumor growth and sensitization to checkpoint blockade in established pancreatic adenocarcinoma preclinical mouse models.
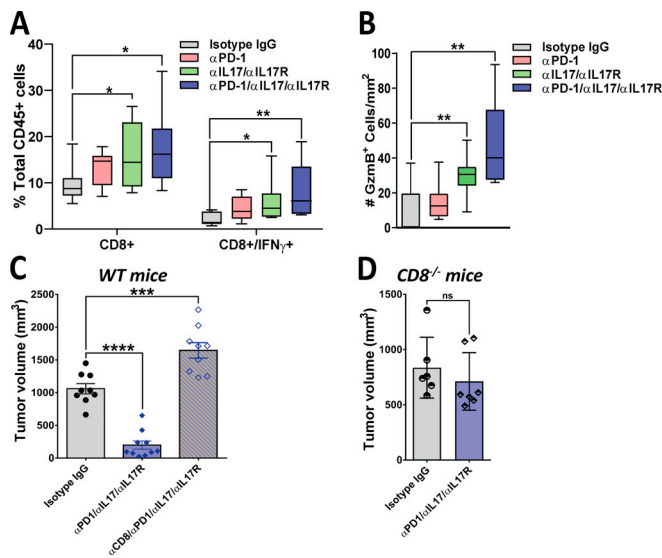
Antitumoral effect of combinatorial IL17/IL17R and PD-1 blockade is CD8^{+} T cell dependent

To further understand the mechanisms behind the antitumoral synergistic effects of IL17/IL17R and PD-1 inhibition, we quantified effector immune cells in orthotopic tumors. We found that combinatorial treatment with anti-IL17/IL17R and anti–PD-1 antibodies significantly affected recruitment of CD8^{+} T cells, in particular cytotoxic IFNγ-secreting CD8^{+} T cells compared with the control treatment arm (Fig. 5 A). We also detected increased CD8^{+} T cell activation as measured by the number of tumor-infiltrating cells expressing granzyme B with combinatorial IL17/IL17R and PD-1 blockade (Fig. 5 B and Fig. S2 C). We then performed correlation analysis between tumor volume and number of CD8^{+} T cells in the four treatment arms. We found no correlation between these two variables in the control and single-antibody treatment arms, but found an inverse correlation between tumor volume and CD8^{+} T cells in mice treated with combinatorial anti-IL17/IL17R/anti–PD-1 ($r = -0.77$), suggesting that T cells are only functionally active in tumors from this treatment arm (Fig. S2 D).

Based on these results, we then hypothesized that CD8^{+} T cells are the mediators of the antitumoral effect induced by IL17/IL17R and PD-1 antibodies. To test this hypothesis, we used neutralizing antibodies against CD8 (rat antimouse; Bio X Cell) on tumor-bearing mice treated with anti-IL17 and anti–PD-1 antibodies. Blockade of CD8 resulted in the loss of efficacy of the IL17/IL17R/PD-1 combination when compared with mice that received the combination plus control IgG isotype (Fig. 5 C). For further validation of these results, we used CD8-deficient mice as recipients of KPC cells and found that the combination of antibodies against IL17/IL17R and PD-1 was not effective in reducing tumor size in the absence of CD8^{+} T cells (Fig. 5 D). These findings strongly indicate that the antitumoral synergistic effect of IL17 blockade and anti–PD-1 agents is mediated by CD8^{+} T cells.

Combinatorial IL17/IL17R and PD-1 inhibition induces metabolic changes that can serve as an activity biomarker

In an attempt to find early biomarkers of activity for the combination of IL17 and checkpoint blockade, we performed RNA sequencing on PDAC orthotopic tumors from mice exposed to IL17/IL17/PD-1 neutralizing antibodies versus IgG isotype in vivo

Figure 5. **The antitumoral effect of combinatorial IL17 and PD-1 blockade is CD8+ T cell dependent. (A)** Flow cytometry–based analysis of tumor-infiltrating CD8+ and CD8+IFNγ+ cells. Tumors were obtained from syngeneic mice orthotopically implanted with KPC cells and treated with isotype IgG, aPD-1, aIL17/aIL17R, or aIL17/aIL17R/aPD-1 antibodies (n = 10 mice/group). Results are expressed as the percentage of total CD45+ gated viable cells. **(B)** IHC-based quantification of tumor-infiltrating cells expressing granzyme B (GzmB+) in tumors from A. Results are expressed as the total number of cells/mm². **(C)** Tumor volumes of orthotopically implanted KPC cells into WT syngeneic mice treated with isotype IgG, anti-IL17/IL17R/PD-1, or anti-CD8 antibodies (aCD8; n = 10). **(D)** Tumor volumes of orthotopically implanted KPC cells into CD8-deficient (CD8−/−) syngeneic mice treated with isotype IgG or anti-IL17/IL17R/PD-1 antibodies (n = 6–7 mice/group). *, P < 0.05; **, P < 0.01; ***, P < 0.001; ****, P < 0.0001; ns, not significant.

(Table S2). We examined differentially regulated genes using Ingenuity Pathway Analysis and found that the combination of IL17/IL17R and PD-1 blockade regulates genes belonging to several metabolic pathways, such as lipid, nucleic acid, carbohydrate, protein, vitamin, and mineral metabolism (Fig. S4 A). Based on these results, and in an attempt to search for biomarkers, we performed ex vivo ¹H nuclear magnetic resonance (NMR) spectroscopy–based metabolomics on freshly explanted pancreatic tumors from the different treatment arms. After detailed analysis of a panel of 16 metabolites, we found that the levels of choline, phosphocholine, glycerophosphocholine, glycine, and lactate were significantly decreased in tumors from mice treated with combinatorial IL17/IL17R/PD-1 blockade, whereas acetate was increased only in tumors from the combination arm (Fig. S4, B and C). We focused on lactate for further validation, given the potential for systemic assessment. Because lactate is primarily indicative of cellular proliferation rate, we assessed if levels were affected early in the treatment when tumors from all treatment arms were of similar size. To this end, we made an assessment 10 d after treatment initiation, when tumors from all treatment arms had similar size (Fig. S3, A and B), and we found that lactate levels in the tumors were significantly lower upon treatment with the combination of IL17/IL17R/PD-1 antibodies even at this early time point, suggesting that lactate changes may precede tumor size changes (Fig. S4, D

and E). We then tested if tumor changes in lactate can be detected systemically and found a significant decrease in serum lactate in the combination arm at 14 and 28 d (Fig. S4, F and G). However, the changes in systemic lactate were similarly decreased in all treatment groups (IL17 blockade, checkpoint blockade, and combination), suggesting lower specificity in this assay than with NMR.

These findings suggest that the changes in the tumor microenvironment induced by IL17 and PD-1 neutralization cause early metabolic changes, which could serve as biomarkers of activity. These findings present a potential early metabolic pharmacodynamic biomarker of target engagement for this novel combinatorial immunotherapy.

Neutrophils and NETosis mediate IL17 immunosuppressive effect in PDAC

Because all the immunoprofiling and transcriptomic assays (CyTOF, single and multiplex IF, IHC, flow cytometry, RNA sequencing) pointed toward neutrophils as the main cell type modulated by IL17, we focused on neutrophils for deeper mechanistic characterization. To determine if neutrophils are mediating the effect of IL17, we performed in vivo depletion of neutrophils in the orthotopic mouse model using neutralizing antibodies against Ly6G (rat antimouse; Bio X Cell). Validation of this antibody by flow cytometry in digested single cells collected from tumors confirmed specific deletion of Ly6G+ cells (Fig. S5, A and B). Interestingly, PD-L1 is increased in tumors upon neutrophil depletion, as seen with IL17 blockade (Figs. S5 C and S1 F). Experiments using mAb against Ly6G as a single agent showed a significant delay in orthotopic tumor growth compared with IgG isotype treatment and a synergistic effect when Ly6G was combined with anti–PD-1 antibodies (Fig. 6 A).

We then asked which specific neutrophil function/pathway is responsible for maintaining immunosuppression and resistance to immunotherapy. It has previously been described that IL17 induces pancreatitis through formation of peptidyl arginine deiminase type IV (Padi4)–dependent neutrophil aggregates (Leppkes et al., 2016; Murthy et al., 2019). Neutrophils use histone citrullination by Padi4 to release decondensed chromatin as neutrophil extracellular traps (NETs) to entrap pathogens, and this process is called "NETosis" (de Bont et al., 2019; Brinkmann et al., 2004). The goal of NETosis is to capture and kill bacteria or other pathogens, but NETs have also been detected in tumors (Cedervall and Olsson, 2016) and have been linked to promotion of cancer metastasis (Park et al., 2016; Rayes et al., 2019). When we looked at genes directly regulated by IL17 in KPC cells (RNA sequencing), we found upregulation of several genes associated with neutrophil recruitment, regulation, or induction of NETosis, including Lcn2, Ltf, Cxcl5, Cxcl3, Csf3, Ltbp2, Duoxa1, Rab15, Noxa1, Tnf, Cbr2, and Il6 (Fig. S1 D; Bennouna et al., 2003; Brandes et al., 1991; Cai et al., 2010; Chen et al., 2016; Ciaffoni et al., 2015; Folco et al., 2018; Francis et al., 2011; Hsu et al., 2019; Jiménez-Alcázar et al., 2015; 2017; Jin et al., 2014; Joshi et al., 2013; Klein et al., 2014; Lee et al., 2011; Li et al., 2018; Lin et al., 2007; Liu et al., 2019; Makhezer et al., 2019; Neeli et al., 2009; Nograles et al., 2008; Okubo et al., 2016; Rada and Leto, 2008; Rouault et al., 2013; Toussaint et al., 2017; Uriarte et al., 2008;
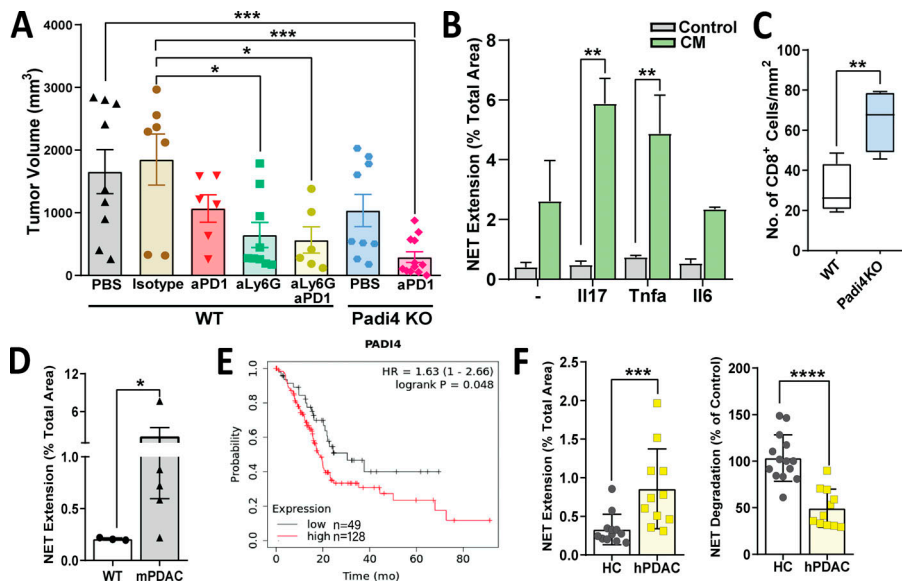
Figure 6. **Tumor-promoting role of neutrophils and NETs during pancreatic cancer.** **(A)** Tumor volume of orthotopic KPC tumors in syngeneic WT mice treated with PBS, isotype IgG, anti–PD-1, anti-Ly6G, or anti-Ly6G/anti–PD-1 or in PADi4-KO mice treated with PBS and anti–PD-1 according to the experimental protocol in Fig. 2 A. **(B)** NET extension of murine neutrophils upon direct stimulation with cytokines (Il17, Tnfα, Il6; control) or with CM from KPC cells stimulated in vitro with the indicated cytokines. NET extension is measured as the percentage of SYTOX Green staining of the total area. The experiment was performed in duplicates for n = 3. **(C)** Quantification of CD8+ cells measured in WT and Padi4-KO tumors from A by IHC. Results are expressed as the total number of cells/mm². **(D)** NET formation of control WT murine neutrophils upon treatment with WT or murine PDAC (KPC) serum. **(E)** Kaplan-Meier survival curves comparing overall survival of patients with PDAC with low versus high levels of median PADI4 expression. **(F)** NET formation (left) and NET degradation (right) of control human neutrophils upon treatment with serum of healthy control subjects (HC) or patients with PDAC. *, $P < 0.05$; **, $P < 0.01$; ***, $P < 0.001$; ****, $P < 0.0001$.

Wang et al., 2009). Through an in vitro NETosis formation assay, we found that although direct addition of recombinant murine IL17 to ex vivo murine control neutrophils in culture does not alter NETosis, conditioned medium (CM) from KPC cells previously exposed to IL17 is much more potent in inducing NETosis when added to control neutrophils (Fig. 6 B).

To test if induction of IL17-driven NETs is the mechanism that mediates immunosuppression in pancreatic cancer, we used the mice deficient in Padi4 (Padi4-KO) as recipients of orthotopic KPC tumors. Although orthotopic implantation of tumors in these mice resulted in only mild and nonsignificant reduction in tumor growth (Fig. 6 A), these mice had a significant increase in CD8+ T cell recruitment to tumors (Fig. 6 C), and addition of PD-1 blockade to Padi4-KO mice had a dramatic effect in tumor reduction (Fig. 6 A). To determine if NETosis is also induced systemically in vivo, we performed functional assays using serum from WT and KPC transgenic mice. We found that serum from KPC mice with pancreatic tumors resulted in a significant increase in NETosis on ex vivo WT neutrophils, as measured by NET extension (Fig. 6 D).

To determine if PADI4-dependent NETosis is relevant in human pancreatic cancer, we examined TCGA data and found that higher expression of PADI4 in patients with PDAC is associated with shorter median survival (HR, 1.63; P = 0.048; Fig. 6 E). We then incubated serum from patients with pancreatic cancer and healthy control subjects with ex vivo control neutrophils isolated from healthy control subjects and measured the potential of these serum samples to induce NET extension and degradation. Interestingly, we found that serum from patients with PDAC significantly increased NET formation while substantially reducing NET degradation (Fig. 6 F and Fig. S5 D). A recent publication found that NETs are an independent prognostic

factor in PDAC and postulated that NETs be added to the TNM (tumor, node, metastasis) staging criteria to improve accuracy of risk stratification and survival prediction (Jin et al., 2019). Altogether, we found that IL17 promotes immunosuppression and resistance to immune checkpoint blockade by inducing neutrophil infiltration and NETs in pancreatic tumors through factors released from cancer cells.

Discussion

The tumor microenvironment surrounding pancreatic cancer is very complex, and several mechanisms contribute to the initiation and maintenance of its immunosuppression. There is an urgent need to determine the factors that trigger those mechanisms because this knowledge can help in the design of efficient strategies to favor antitumoral immunity and can provide a rationale for synergistic combinatorial immunotherapies for this highly lethal cancer.

IL17 has a protumorigenic role in the initiation and progression of pancreatic premalignant lesions, and, in this study, we focus on unraveling the role of IL17 in established cancer. We showed that the absence of IL17/IL17R signaling on epithelial cancer cells by genetic manipulation dampens in vivo tumor growth significantly, whereas mAb against IL17 did not show the same efficacy as single agents. This may be explained by several possibilities, such as the lower efficacy of pharmacological neutralization versus complete genetic deletion; interaction of IL17 antibodies with nontumoral or nonepithelial cells, resulting in reduction of the antitumorigenic effect; and a potential microbial gut-driven IL17/IL17RA positive feedback that would result in higher levels of circulating IL17A, diminishing the antibody-mediated inhibition locally in the tumor.

Zhang et al.
IL17-induced NETs and immunosuppression in PDAC

Journal of Experimental Medicine   7 of 14
https://doi.org/10.1084/jem.20190354

Through a combination of immunoprofiling methodologies (CyTOF, RNA sequencing, flow cytometry, and immunohistochemical and multiplex IF analysis), we found that IL17 blockade inhibits neutrophil recruitment to the tumors and specifically increases activated, cytotoxic CD8+ T cells, which are spatially localized closer to tumor cells. Despite this potent immunomodulation induced by IL17-neutralizing antibodies, they were not capable of inducing antitumoral efficacy as single agents. This study has identified therapeutic synergism between IL17 and PD-1 inhibition using pharmacological and CRISPR/Cas9-based genetic approaches in different preclinical models of PDAC. We have also shown that these results are not restricted to anti–PD-1, because the combination of IL17 and CTLA4 antibodies was also synergistically effective against PDAC. Furthermore, using pharmacological and genetic suppression of CD8+ T cells, we found that the synergistic effect of combining IL17 and PD-1 inhibition is dependent on CD8+ T cell activation. When looking at changes induced by the combination treatment at the mRNA level, we found several metabolic pathways were involved, and therefore we explored metabolic biomarkers by NMR spectroscopy and found lactate as an early predictor of responses to combination immunotherapy (Fig. S4). These data suggest that, considering the delayed tumor responses usually seen with immunotherapies, we could use metabolic imaging methods that rely on lactate measurements (e.g., positron emission tomography, MRI-based hyperpolarization) for early prediction of responses to anti-IL17/PD-1 activity. This is particularly important for immunotherapies that usually have delayed antitumoral efficacy by standard imaging methodologies (Borcoman et al., 2018).

We also demonstrated that IL17 potentiates its immunosuppressive effects through recruitment of tumor-associated neutrophils and induces its pathogen clearance mechanism of NETosis. Blockade of either neutrophils or Padi4-dependent NETosis synergizes with PD-1 blockade to dramatically reduce tumor growth (Fig. 6). It should be noted that neutrophil depletion was done with anti-Ly6G antibodies, which can also deplete MDSCs, and therefore the potential role of these cells in mediating some of the effects described cannot be discarded.

These findings were somewhat unexpected because previous studies have described neutrophils and NETosis as contributors to adaptive immunity by activating plasmacytoid dendritic cells and inducing T cell priming (Tillack et al., 2012; Beauvillain et al., 2007). However, this function may be context dependent, depending on the type of tumor and microenvironment. To this effect, a study that explored the role of NETs in Ewing sarcoma determined that in this tumor type, the presence of NETs was associated with worse prognosis (Berger-Achituv et al., 2013). We have found that spatial remodeling, including mobilization of CD8+ T cells upon IL17 blockade, results from decreased neutrophil infiltration. NETs may be forming a physical and functional barrier that separates cancer cells from immune cells, favoring tumor growth due to lack of immune recognition.

With respect to IL17, it is peculiar that this cytokine plays such a pivotal role during pancreatic cancer. IL17 is primarily secreted by Th17 cells, which accumulate in the gastrointestinal tract under homeostatic conditions in the presence of specific commensal and pathogenic bacteria such as segmented filamentous bacteria (Ivanov et al., 2008, 2009). Interestingly, recent emerging evidence developed by our group and others has implicated the role of gut and intratumoral microbiota in pancreatic tumorigenesis through modulation of immune responses (Pushalkar et al., 2018; Riquelme et al., 2018, 2019). It remains to be explored whether IL17 responses can be induced either locally by intratumoral bacteria or systemically by gut bacteria, leading to protumorigenic effects via tumor-associated neutrophils during pancreatic cancer. It is possible that, inadvertently through this mechanism, the neutrophils may be contributing to a fibrotic and immunosuppressive stroma during PDAC.

We anticipate that the combination of anti–PD-1 and anti-IL17 antibodies will translate to the clinic, given commercial availability and US Food and Drug Administration approval of anti-IL17 antibodies. Currently, a fully human mAb against IL17A, secukinumab, is approved for treatment of moderate to severe plaque psoriasis (Langley et al., 2014; Pariser et al., 2018; Gottlieb et al., 2015). A human anti-IL17RA mAb is brodalumab, which blocks IL17RA as well as the binding of its receptor ligands: IL17A, IL17F, and IL17E (Lebwohl et al., 2015). Brodalumab has proved to have significant clinical benefit and an acceptable safety profile, but it has been linked to depression and increased suicide risk, whereas this was not found with anti-IL17A agents (Strober et al., 2018; Reich et al., 2017). One could imagine that combination therapy with anti-IL17 agents together with checkpoint inhibitors could potentially result in increased toxicities, as well as off-target effects, and these aspects would have to be studied in the context of a trial, which would be justified in light of the present data, the severity of pancreatic cancer, and the mild efficacy of most treatment modalities.

In conclusion, given the presented clinical data, mechanistic implications, and potentially acceptable safety profile, the immediate translation of IL17 inhibitors for pancreatic cancer should be warranted. Interestingly enough, the ongoing COVID-19 viral pandemic has been characterized with hyperinflammation and microthrombosis associated with cytokine release syndrome, which includes secretion of IL17 (Guan and Zhong, 2020; Xu et al., 2020; Huang et al., 2020; Klok et al., 2020a, 2020b; Grasselli et al., 2020; Magro et al., 2020). Additionally, NETosis is increased in patients with severe COVID-19 and has been postulated to aggravate the disease (Barnes et al., 2020; Zuo et al., 2020). Because our study demonstrates that IL17 is a potent inducer of NETosis through epithelial cell signaling, we hypothesize that IL17 plays a key role in promoting COVID-19 pathogenesis through induction of systemic NETosis by contributing to the cytokine storm and microthrombotic events. We propose to repurpose clinically approved human mAb against IL17 for use in critically ill COVID-19 patients.

Materials and methods

Cell lines

Murine pancreatic adenocarcinoma cells derived from a spontaneous tumor in a KPC mouse were used and named "KPC" cells. Cells were cultivated in DMEM with 4.5 g/liter glucose

(Mediatech) supplemented with 10% FBS (Sigma-Aldrich) and 1% penicillin-streptomycin (HyClone Laboratories) at 37°C and 5% CO_2 in a humidified atmosphere. sMT3 cells were kindly provided by David Tuveson (Cold Spring Harbor Laboratory, Cold Spring Harbor, NY). Targeted knockout of IL17RA in KPC cells was performed using a CRISPR/Cas9-mediated genome editing kit (Santa Cruz Biotechnology) with mouse IL17R CRISPR/Cas9 plasmid (sc-421093) and mouse IL17R HDR plasmid (sc-421093-HDR) following the manufacturer's instructions. GFP/RFP-positive cells were plated into 96-well plates with single-cell sorting. IL17RA-KO clones were confirmed by Western blotting with two antibodies: anti-IL17R [H-168] (sc-30175; Santa Cruz Biotechnology) and anti-IL17RA [EPR1544(2)] (ab134086; Abcam).

Animal models
All animal experiments were conducted in compliance with the National Institutes of Health guidelines for animal research and were approved by the Institutional Animal Care and Use Committee of The University of Texas MD Anderson Cancer Center. C57BL/6 mice purchased from Taconic Biosciences were used for most experiments. CD8-KO and Padi4-KO mice were purchased from The Jackson Laboratory. For orthotopic PDAC mouse models, 8-wk-old male mice were anesthetized by inhalation of 2% isoflurane in oxygen. An incision was made on the left side of the mouse to exteriorize the pancreas. 10^5 KPC cells in 10 µl PBS/Matrigel (Corning; vol/vol, 1:1) were injected into the pancreas. The incision was closed with 6-0 polyglycolic acid sutures (CP Medical). For subcutaneous models, 5×10^5 KPC cells in 100 µl PBS/Matrigel (vol/vol, 1:1) were injected into the mouse flank subcutaneously. Tumor volume was calculated as length × width × width/2 in cubic millimeters.

Neutralizing antibody administration and randomization
Neutralizing antibodies against mouse IL17, IL17R, IL17E (generously provided by Amgen), PD-1, CD8a, Ly6G, and rat IgG (Bio X Cell). Doses, frequencies, species in which antibodies were raised, reactivity, and injection mode are tabulated in Table S3. All antibody-based neutralization treatments were started not earlier than 10 d following KPC cell implantation and only in mice with tumor volume larger than 100 mm³ (as measured by ultrasound/MRI in the orthotopic model and manually measured with calipers in the subcutaneous model). We have included MRI photos of mice from the orthotopic model randomized to the four treatment arms and tumor volume quantification at day 10 after implantation (Fig. S3, A and B).

Histopathology
Tumor-bearing mice were humanely sacrificed, and the pancreas or implanted tumor was excised and then fixed in freshly prepared 4% paraformaldehyde in PBS, pH 7.2. Tissues were embedded in paraffin, and 5-µm sections were obtained and stained with hematoxylin (Dako) and eosin (VWR) following standard protocols for visual examination. The stained slides were reviewed and screened for representative tumor regions by a pathologist.

Serum mouse cytokines, chemokines, and growth factor detection
Analysis of cytokines was done on the serum of 1-mo-old and 6-mo-old KPC and Cre mice. A mouse Th1/Th2/Th17 cytokine array kit (560485 and 551287; BD Biosciences) was used with 50 µl of serum. The capture of cytokines from serum was done according to the manufacturer's instructions, and captured cytokines were analyzed using BD FACSCanto II (BD Biosciences). Instrument parameters were set up according to the instructions provided in the manufacturer's manual. Data were analyzed using FCAP Array Software (BD Biosciences).

CyTOF
KPC orthotopic tumors were treated with isotype IgG or anti-IL17/17R neutralizing antibodies for 2 wk. Tumor tissues were harvested and digested with collagenase P, and single-cell suspensions were stained with 5 µM Cell-ID Cisplatin (Fluidigm Corp.) and incubated with Fc block (BD Biosciences), followed by surface antibody cocktail. Antibody details including final concentrations can be found in Table S3. Next, cells were washed and fixed in Maxpar Fix I buffer (Fluidigm Corp.) and barcoded using the Cell-ID 20-Plex Pd Barcoding Kit (Fluidigm Corp.). Next, the cells were incubated with intracellular antibody cocktail, washed, and stained with 1.25 µM Cell-ID Intercalator-Ir (Fluidigm Corp.). Sample acquisition was performed on a Helios mass cytometer (Fluidigm Corp.). The analysis was performed with FlowJo version 10 software (FlowJo LLC).

Human pancreatic tumor microarrays
Human pancreatic adenocarcinoma and normal tissue microarrays were collected and made by The University of Texas MD Anderson Cancer Center. The study protocol for tissue collection and use was approved by the institutional review board of The University of Texas MD Anderson Cancer Center.

RNA isolation and quantitative RT-PCR
KPC cells were stimulated with 10 ng/ml murine recombinant IL17 proteins for 7 d (R&D Systems). Total RNA was extracted with the RNeasy RNA isolation kit (Qiagen) and reverse transcribed with a cDNA Reverse Transcription Kit (Applied Biosystems). Quantitative RT-PCR was performed with Fast SYBR Green Master Mix (Applied Biosystems) on a ViiA 7 real-time PCR system (Applied Biosystems). Sequences of all validated PCR primers were obtained from PrimerBank (https://pga.mgh.harvard.edu/primerbank/), and primers were synthesized by Sigma-Aldrich. GAPDH was used for normalization. Assays were run in triplicate.

RNA sequencing
KPC orthotopic PDAC mouse models were treated with isotype IgG or anti-IL17/IL17R neutralizing antibodies for 2 wk. Total RNA was extracted from tumor tissues. Each sample was assessed using a Qubit 2.0 fluorometer and Agilent TapeStation 2200 for RNA quantity and quality. Then sequencing was performed on an Illumina NextSeq 500s, as previously described. Sequencing analysis was done using mRNA-sequencing analysis on the Maverix Analytic Platform (Maverix Biomics, Inc.). RNA

Zhang et al.
IL17-induced NETs and immunosuppression in PDAC

Journal of Experimental Medicine   9 of 14
https://doi.org/10.1084/jem.20190354

sequencing data are being deposited in the Sequence Archive (NCBI SRA under BioProject accession no. PRJNA655914). Data can be found in Table S1 and Table S2.

IHC
Paraformaldehyde-fixed, paraffin-embedded tissue sections were deparaffinized, rehydrated, and then boiled using the EZ-Retriever System (BioGenex) with 0.01 mol/liter citrate buffer, pH 6.0 (Sigma-Aldrich), for antigen retrieval. Endogenous peroxidases were blocked with 0.3% H_2O_2 for 15 min. Nonspecific epitopes were blocked with 10% normal goat serum (Seracare Life Sciences) for 30 min. The sections were incubated overnight at 4°C with antibodies against mouse CD8a, Gzmb, Ly6G, cleaved caspase 3 and Ki-6, and human CD15 and RORγt. Antibody details, including final concentrations, can be found in Table S3. This was followed by using a SignalStain Boost IHC Detection Reagent and DAB Substrate Kit (Cell Signaling Technology) following the manufacturer's instructions. Slides were then counterstained with hematoxylin, mounted in Acrymount (StatLab), and visualized under a light microscope.

Opal multiplex IF
Staining was performed manually using the same primary antibodies used for IHC analysis against the immune markers antimouse CD8a, Gr1, SMA, Gzmb, and CK19 mAb. Staining was performed consecutively by using the same steps used in IHC, and the detection for each marker was completed before application of the next antibody. Details on primary antibodies are found in Table S3. The Opal Polymer HRP Ms + Rb detection reagent (PerkinElmer) was used for the primary antibody detection, and Opal 7-Color Manual IHC was used with six reactive fluorophores: Opal 520, Opal 540, Opal 570, Opal 620, Opal 650, and Opal 690 plus DAPI nuclear counterstain, according to the manufacturer's instructions (NEL811001KT; PerkinElmer). Uniplex IF and negative control were stained with the same protocols. Slides were imaged using the Vectra 3.0 spectral imaging system (PerkinElmer) according to previously published instructions.

Quantification of multiplex images
The L function was calculated with the R language using the formula $L(r) = \sqrt{\left[\frac{K(r)}{\pi}\right]}$, as previously published (Carstens et al., 2017). For the proximity analysis, we obtained positions of all cellular phenotypes and recorded them in a text file (PerkinElmer). We then used MATLAB to determine relative distance between cellular types. We calculated cn_{AB}, which is the total number of cells with phenotype B positioned within a fixed radius of cells with phenotype A. The phenotypes A and B we analyzed were CD8+, CD8+GzmB+, CK19+, GR1+, GzmB+, other, and SMA+. The program computed the Euclidean distance $d(C_1, C_2)$ between a pair of cells C_1 and C_2 with phenotypes A and B, respectively, where $C_{i,x}$ and $C_{i,y}$ are the x and y coordinates of cell C_i for $i = 1, 2$.

$$d(C_1, C_2) = \sqrt{(C_{1,x} - C_{2,x})^2 + (C_{1,y} - C_{2,y})^2}$$

This count yields n_{AB}, which is the number of near pairs. The number of near pairs was calculated among the four treatment groups, and the average number was plotted.

Flow cytometry
Tumor tissues were harvested and digested into single-cell suspensions by collagenase P. The obtained cells were stained with rat antimouse CD45, CD4, Foxp3, Ly-6G, IFN-γ, and CD8a antibodies. Antibody details, including final concentrations, can be found in Table S3. Sample acquisition was performed on an LSRFortessa X-20 Analyzer flow cytometer (BD Biosciences). The analysis was performed with FlowJo version 10 software (FlowJo LLC).

Lactate measurements
Mouse sera from PDAC models or cell culture medium were collected, and lactate levels were measured using the Lactate Colorimetric/Fluorometric Assay Kit (BioVision). Assays were run in triplicates.

Ex vivo ¹H NMR spectroscopy
Each tumor sample was weighed, crushed, and immersed in 3 ml of a methanol-to-water mixture (2:1) on top of 0.5 ml of polymer vortex beads inside a 15-ml tube. Mechanical homogenization was performed by vortexing the tubes for 15 s, flash freezing in liquid nitrogen for 1 min, and allowing the mixture to thaw, repeated three times. The samples were then centrifugated for 10 min to separate the water-soluble metabolites from proteins and other cellular constituents. Supernatant was extracted and subjected to rotary evaporation to remove the methanol. Samples were further desiccated overnight with a lyophilizer, leaving just the collection of metabolites. Metabolites were then dissolved in a solution of 600 μl $2H_2O$, 36 μl PO_4 buffer, and 4 μl 80 mM 4,4-dimethyl-4-silapentane-1-sulfonic acid (DSS). Phosphate buffer was added to stabilize any potential pH variations, and DSS served as the reference standard to which we normalized the spectral signal from each metabolite.

NMR spectra were obtained using a Bruker AVANCE III HD NMR scanner (Bruker Biospin Corporation) at 298 K. The spectrometer operates at a ¹H resonance frequency of 500 MHz and is endowed with a triple-resonance (¹H, ¹³C, ¹⁵N) cryogenic temperature probe with a z axis shielded gradient. A presaturation technique was implemented for water suppression. Spectra were obtained with a 90° pulse width, a scan delay t_{rel} of 6.0 s, a 1,024-Hz spectral width, and an acquisition time t_{max} of 1.09 s (16,000 complex points). A total of 256 scans were collected and averaged for each spectrum, which resulted in a total scan time of 32 min, 49 s. Here, $t_{rel} + t_{max}$ was nearly 8 s, so that it was greater than $3*T_1$ of the metabolites observed. The time domain signal was apodized using an exponential function. After the spectra were acquired, metabolic profiling was performed using Chenomx NMR Suite 8.1 software (Chenomx Inc.). Quantification of the metabolites was then performed using MestReNova software (Mestrelab Research) by integrating a nonzero region centered on the chemical shift at which the metabolite is known to resonate. This integral value for each metabolite is then normalized by the value of the integral of the DSS reference peak.

Isolation of neutrophils
Neutrophils were isolated by density gradient centrifugation from peripheral whole blood (Gonzalez et al., 2014) from WT

mice. 7 ml of whole blood was overlaid on 7 ml Histopaque 1119 (Sigma-Aldrich) in a 15-ml conical tube and centrifuged at 800 ×g for 20 min at room temperature with no brakes. The upper phases containing serum, lymphocytes, and monocytes were discarded and the lower polymorphonuclear layer above the RBC pellet was transferred to another tube and washed in PBS. A Percoll gradient (Sigma-Aldrich) was created by layering 2 ml each of 85%, 80%, 75%, 70%, and 65% isotonic Percoll solution, starting with the 85% layer at the bottom of a 15-ml conical tube. Cells from the previous step were resuspended in 2 ml PBS, laid on top of the 65% layer, and centrifuged at 800 ×g for 20 min at room temperature with no brakes. Cells at the 75–70% interphase were harvested and washed in PBS. Cells were resuspended in phenol red–free RPMI, 10 mM Hepes, and 0.5% BSA (HyClone Laboratories).

Human neutrophils were isolated using the same protocol from healthy control patients, under University of Texas MD Anderson Cancer Center–approved institutional review board protocols, and resuspended in phenol red–free RPMI, 10 mM Hepes, and 0.5% human serum albumin (Sigma-Aldrich).

NETosis assay

5×10^5 KPC cells were seeded per well of a six-well plate in phenol red–free DMEM (Invitrogen) and stimulated for 24 h with 10 ng/ml of murine recombinant Il17, Tnfα, and Il6 proteins (R&D Systems). Neutrophils were isolated from WT mice as described above, and 2×10^5 neutrophils/well were seeded in a 24-well tissue culture plate. For NET formation assays, the neutrophils were allowed to adhere for ∼20 min, and then CM from KPC cells was added. After 24 h, 200 nM SYTOX Green (Invitrogen) in HBSS was carefully added to the plate without disturbing the NETs. After 15 min, the plate was imaged with an Olympus IX70 fluorescence microscope. Five fields of view at 10× magnification were captured for each well. The analysis was done using ImageJ software (National Institutes of Health). NET extension was calculated as the percentage of the total area covered by the SYTOX Green–positive area.

For human studies, serum was collected from healthy control subjects and patients with PDAC or from WT and KPC mice and stored at –80°C until further use. The study protocols were approved by the institutional review board at The University of Texas MD Anderson Cancer Center. For serum-based NETosis assays, 10% serum was added to freshly isolated neutrophils and incubated at 37°C. After 2 h, 200 nM SYTOX Green (Invitrogen) was added and imaged as described above. For NET degradation, neutrophils were first allowed to form NETs by incubation with 50 nM PMA (Sigma-Aldrich) for 2 h at 37°C. Then the stimulation was removed, and 10% serum was added to each well and incubated for 6 h at 37°C. To stop the nuclease activity, 2 mM EDTA (Invitrogen) was added, and DNA content in the supernatant was fluorescently measured with the PicoGreen kit (Invitrogen) using the Synergy HTX microplate reader (BioTek Instruments Inc.). DNA released by control samples was considered as 100% NET degradation.

Statistical analysis

Data were expressed as the mean ± SD. Data were analyzed using Prism software (GraphPad Software, Inc.). Statistical significance between two groups was assessed using a two-sample t test assuming unequal variances. When more than two value sets were compared, we used one-way ANOVA followed by the Dunnett test when the data involved three or more groups. $P < 0.05$, $P < 0.01$, $P < 0.001$, or $P < 0.0001$ was considered statistically significant.

The Kaplan-Meier curves in Figs. 1 D and 6 E were generated using TCGA RNA-sequencing data from the KM-plotter webtool as previously reported (Lánczky et al., 2016). Higher and lower expression levels were stratified on the basis of median expression levels. Statistical analysis was performed using log-rank tests, and HRs were calculated.

Online supplemental material

Fig. S1 shows the immunological and antitumoral effects of IL17 blockade with and without anti–PD-1 blockade. Fig. S2 shows multiplex IF characterization of the tumor microenvironment. Fig. S3 shows the antitumoral effect of the combination of IL17 and PD-1 blockade in orthotopic tumors. Fig. S4 shows the tumor metabolic changes with the combination of IL17 and PD-1 blockade. Fig. S5 shows neutrophil depletion and NETosis imaging with human samples. Table S1 shows RNA sequencing of tumors from mice treated with isotype IgG versusaIL17/IL17R mAb. Table S2 shows RNA sequencing of tumors from mice treated with isotype IgG versusaIL17/IL17R + anti–PD-1 blockade. Table S3 provides reagent information.

References

Balachandran, V.P., G.L. Beatty, and S.K. Dougan. 2019. Broadening the impact of immunotherapy to pancreatic cancer: Challenges and opportunities. *Gastroenterology*. 156:2056–2072. https://doi.org/10.1053/j.gastro.2018.12.038

Barnes, B.J., J.M. Adrover, A. Baxter-Stoltzfus, A. Borczuk, J. Cools-Lartigue, J.M. Crawford, J. Daßler-Plenker, P. Guerci, C. Huynh, J.S. Knight, et al. 2020. Targeting potential drivers of COVID-19: Neutrophil extracellular traps. *J. Exp. Med*. 217. e20200652. https://doi.org/10.1084/jem.20200652

Bayne, L.J., G.L. Beatty, N. Jhala, C.E. Clark, A.D. Rhim, B.Z. Stanger, and R.H. Vonderheide. 2012. Tumor-derived granulocyte-macrophage colony-stimulating factor regulates myeloid inflammation and T cell immunity in pancreatic cancer. *Cancer Cell*. 21:822–835. https://doi.org/10.1016/j.ccr.2012.04.025

Beauvillain, C., Y. Delneste, M. Scotet, A. Peres, H. Gascan, P. Guermonprez, V. Barnaba, and P. Jeannin. 2007. Neutrophils efficiently cross-prime naive T cells in vivo. *Blood*. 110:2965–2973. https://doi.org/10.1182/blood-2006-12-063826

Bennouna, S., S.K. Bliss, T.J. Curiel, and E.Y. Denkers. 2003. Cross-talk in the innate immune system: neutrophils instruct recruitment and activation of dendritic cells during microbial infection. *J. Immunol*. 171:6052–6058. https://doi.org/10.4049/jimmunol.171.11.6052

Berger-Achituv, S., V. Brinkmann, U.A. Abed, L.I. Kühn, J. Ben-Ezra, R. Elhasid, and A. Zychlinsky. 2013. A proposed role for neutrophil extracellular traps in cancer immunoediting. *Front. Immunol*. 4:48. https://doi.org/10.3389/fimmu.2013.00048

Boj, S.F., C.I. Hwang, L.A. Baker, I.I. Chio, D.D. Engle, V. Corbo, M. Jager, M. Ponz-Sarvise, H. Tiriac, M.S. Spector, et al. 2015. Organoid models of human and mouse ductal pancreatic cancer. *Cell*. 160:324–338. https://doi.org/10.1016/j.cell.2014.12.021

Borcoman, E., A. Nandikolla, G. Long, S. Goel, and C. Le Tourneau. 2018. Patterns of response and progression to immunotherapy. *Am. Soc. Clin. Oncol. Educ. Book*. 38:169–178. https://doi.org/10.1200/EDBK_200643

Brahmer, J.R., S.S. Tykodi, L.Q. Chow, W.J. Hwu, S.L. Topalian, P. Hwu, C.G. Drake, L.H. Camacho, J. Kauh, K. Odunsi, et al. 2012. Safety and activity of anti-PD-L1 antibody in patients with advanced cancer. *N. Engl. J. Med*. 366:2455–2465. https://doi.org/10.1056/NEJMoa1200694

Brahmer, J., K.L. Reckamp, P. Baas, L. Crinò, W.E. Eberhardt, E. Poddubskaya, S. Antonia, A. Pluzanski, E.E. Vokes, E. Holgado, et al. 2015. Nivolumab versus docetaxel in advanced squamous-cell non-small-cell lung cancer. *N. Engl. J. Med*. 373:123–135. https://doi.org/10.1056/NEJMoa1504627

Brandes, M.E., U.E. Mai, K. Ohura, and S.M. Wahl. 1991. Type I transforming growth factor-beta receptors on neutrophils mediate chemotaxis to transforming growth factor-beta. *J. Immunol*. 147:1600–1606.

Brinkmann, V., U. Reichard, C. Goosmann, B. Fauler, Y. Uhlemann, D.S. Weiss, Y. Weinrauch, and A. Zychlinsky. 2004. Neutrophil extracellular traps kill bacteria. *Science*. 303:1532–1535. https://doi.org/10.1126/science.1092385

Cai, S., S. Batra, S.A. Lira, J.K. Kolls, and S. Jeyaseelan. 2010. CXCL1 regulates pulmonary host defense to *Klebsiella* Infection via CXCL2, CXCL5, NF-kappaB, and MAPKs. *J. Immunol*. 185:6214–6225. https://doi.org/10.4049/jimmunol.0903843

Carstens, J.L., P. Correa de Sampaio, D. Yang, S. Barua, H. Wang, A. Rao, J.P. Allison, V.S. LeBleu, and R. Kalluri. 2017. Spatial computation of intratumoral T cells correlates with survival of patients with pancreatic cancer. *Nat. Commun*. 8:15095. https://doi.org/10.1038/ncomms15095

Cedervall, J., and A.K. Olsson. 2016. Immunity gone astray — NETs in cancer. *Trends Cancer*. 2:633–634. https://doi.org/10.1016/j.trecan.2016.10.012

Chao, T., E.E. Furth, and R.H. Vonderheide. 2016. CXCR2-dependent accumulation of tumor-associated neutrophils regulates T-cell immunity in pancreatic ductal adenocarcinoma. *Cancer Immunol. Res*. 4:968–982. https://doi.org/10.1158/2326-6066.CIR-16-0188

Chen, K., T. Eddens, G. Trevejo-Nunez, E.E. Way, W. Elsegeiny, D.M. Ricks, A.V. Garg, C.J. Erb, M. Bo, T. Wang, et al. 2016. IL-17 receptor signaling in the lung epithelium is required for mucosal chemokine gradients and pulmonary host defense against *K. pneumoniae*. *Cell Host Microbe*. 20:596–605. https://doi.org/10.1016/j.chom.2016.10.003

Ciaffoni, F., E. Cassella, L. Varricchio, M. Massa, G. Barosi, and A.R. Migliaccio. 2015. Activation of non-canonical TGF-β1 signaling indicates an autoimmune mechanism of bone marrow fibrosis in primary myelofibrosis. *Blood Cells Mol. Dis*. 54:234–241. https://doi.org/10.1016/j.bcmd.2014.12.005

Clark, C.E., S.R. Hingorani, R. Mick, C. Combs, D.A. Tuveson, and R.H. Vonderheide. 2007. Dynamics of the immune reaction to pancreatic cancer from inception to invasion. *Cancer Res*. 67:9518–9527. https://doi.org/10.1158/0008-5472.CAN-07-0175

D'Angelo, S.P., J. Larkin, J.A. Sosman, C. Lebbé, B. Brady, B. Neyns, H. Schmidt, J.C. Hassel, F.S. Hodi, P. Lorigan, et al. 2017. Efficacy and safety of nivolumab alone or in combination with ipilimumab in patients with mucosal melanoma: a pooled analysis. *J. Clin. Oncol*. 35:226–235. https://doi.org/10.1200/JCO.2016.67.9258

de Bont, C.M., W.C. Boelens, and G.J.M. Pruijn. 2019. NETosis, complement, and coagulation: a triangular relationship. *Cell. Mol. Immunol*. 16:19–27. https://doi.org/10.1038/s41423-018-0024-0

Diaz, L.A., Jr., and D.T. Le. 2015. PD-1 blockade in tumors with mismatch-repair deficiency [letter]. *N. Engl. J. Med*. 373:1979. https://doi.org/10.1056/NEJMc1510353

Eisenhauer, E.A., P. Therasse, J. Bogaerts, L.H. Schwartz, D. Sargent, R. Ford, J. Dancey, S. Arbuck, S. Gwyther, M. Mooney, et al. 2009. New response evaluation criteria in solid tumours: revised RECIST guideline (version 1.1). *Eur. J. Cancer*. 45:228–247. https://doi.org/10.1016/j.ejca.2008.10.026

Feig, C., J.O. Jones, M. Kraman, R.J. Wells, A. Deonarine, D.S. Chan, C.M. Connell, E.W. Roberts, Q. Zhao, O.L. Caballero, et al. 2013. Targeting CXCL12 from FAP-expressing carcinoma-associated fibroblasts synergizes with anti-PD-L1 immunotherapy in pancreatic cancer. *Proc. Natl. Acad. Sci. USA*. 110:20212–20217. https://doi.org/10.1073/pnas.1320318110

Folco, E.J., T.L. Mawson, A. Vromman, B. Bernardes-Souza, G. Franck, O. Persson, M. Nakamura, G. Newton, F.W. Luscinskas, and P. Libby. 2018. Neutrophil extracellular traps induce endothelial cell activation and tissue factor production through interleukin-1α and cathepsin G. *Arterioscler. Thromb. Vasc. Biol*. 38:1901–1912. https://doi.org/10.1161/ATVBAHA.118.311150

Francis, N., S.H. Wong, P. Hampson, K. Wang, S.P. Young, H.P. Deigner, M. Salmon, D. Scheel-Toellner, and J.M. Lord. 2011. Lactoferrin inhibits neutrophil apoptosis via blockade of proximal apoptotic signaling events. *Biochim. Biophys. Acta*. 1813:1822–1826. https://doi.org/10.1016/j.bbamcr.2011.07.004

Gonzalez, A.S., B.W. Bardoel, C.J. Harbort, and A. Zychlinsky. 2014. Induction and Quantification of Neutrophil Extracellular Traps. *In* Neutrophil Methods and Protocols. Methods in Molecular Biology (Methods and Protocols). Vol. Vol. 1124. M. Quinn, and F. DeLeo, editors. Humana Press, Totowa, NJ. https://doi.org/10.1007/978-1-62703-845-4_20

Gottlieb, A.B., R.G. Langley, S. Philipp, B. Sigurgeirsson, A. Blauvelt, R. Martin, C. Papavassilis, and S. Mpofu. 2015. Secukinumab improves physical function in subjects with plaque psoriasis and psoriatic arthritis: results from two randomized, phase 3 trials. *J. Drugs Dermatol*. 14:821–833.

Grasselli, G., A. Zangrillo, A. Zanella, M. Antonelli, L. Cabrini, A. Castelli, D. Cereda, A. Coluccello, G. Foti, R. Fumagalli, et al; COVID-19 Lombardy ICU Network. 2020. Baseline characteristics and outcomes of 1591 patients infected with SARS-CoV-2 admitted to ICUs of the Lombardy region, Italy. *JAMA*. 323:1574–1581. https://doi.org/10.1001/jama.2020.5394

Guan, W.J., and N.S. Zhong. 2020. Clinical characteristics of Covid-19 in China [letter]. *N. Engl. J. Med*. 382:1861–1862.

Herbst, R.S., J.C. Soria, M. Kowanetz, G.D. Fine, O. Hamid, M.S. Gordon, J.A. Sosman, D.F. McDermott, J.D. Powderly, S.N. Gettinger, et al. 2014. Predictive correlates of response to the anti-PD-L1 antibody MPDL3280A in cancer patients. *Nature*. 515:563–567. https://doi.org/10.1038/nature14011

Highfill, S.L., Y. Cui, A.J. Giles, J.P. Smith, H. Zhang, E. Morse, R.N. Kaplan, and C.L. Mackall. 2014. Disruption of CXCR2-mediated MDSC tumor trafficking enhances anti-PD1 efficacy. *Sci. Transl. Med*. 6. 237ra67. https://doi.org/10.1126/scitranslmed.3007974

Hsu, B.E., S. Tabariès, R.M. Johnson, S. Andrzejewski, J. Senecal, C. Lehuédé, M.G. Annis, E.H. Ma, S. Völs, L. Ramsay, et al. 2019. Immature low-density neutrophils exhibit metabolic flexibility that facilitates breast cancer liver metastasis. *Cell Rep.* 27:3902–3915.e6. https://doi.org/10.1016/j.celrep.2019.05.091

Huang, C., Y. Wang, X. Li, L. Ren, J. Zhao, Y. Hu, L. Zhang, G. Fan, J. Xu, X. Gu, et al. 2020. Clinical features of patients infected with 2019 novel coronavirus in Wuhan, China. *Lancet.* 395:497–506. https://doi.org/10.1016/S0140-6736(20)30183-5

Ivanov, I.I., R.L. Frutos, N. Manel, K. Yoshinaga, D.B. Rifkin, R.B. Sartor, B.B. Finlay, and D.R. Littman. 2008. Specific microbiota direct the differentiation of IL-17-producing T-helper cells in the mucosa of the small intestine. *Cell Host Microbe.* 4:337–349. https://doi.org/10.1016/j.chom.2008.09.009

Ivanov, I.I., K. Atarashi, N. Manel, E.L. Brodie, T. Shima, U. Karaoz, D. Wei, K.C. Goldfarb, C.A. Santee, S.V. Lynch, et al. 2009. Induction of intestinal Th17 cells by segmented filamentous bacteria. *Cell.* 139:485–498. https://doi.org/10.1016/j.cell.2009.09.033

Jiménez-Alcázar, M., M. Napirei, R. Panda, E.C. Köhler, J.A. Kremer Hovinga, H.G. Mannherz, S. Peine, T. Renné, B. Lämmle, and T.A. Fuchs. 2015. Impaired DNase1-mediated degradation of neutrophil extracellular traps is associated with acute thrombotic microangiopathies. *J. Thromb. Haemost.* 13:732–742. https://doi.org/10.1111/jth.12796

Jiménez-Alcázar, M., C. Rangaswamy, R. Panda, J. Bitterling, Y.J. Simsek, A.T. Long, R. Bilyy, V. Krenn, C. Renné, T. Renné, et al. 2017. Host DNases prevent vascular occlusion by neutrophil extracellular traps. *Science.* 358:1202–1206. https://doi.org/10.1126/science.aam8897

Jin, L., S. Batra, D.N. Douda, N. Palaniyar, and S. Jeyaseelan. 2014. CXCL1 contributes to host defense in polymicrobial sepsis via modulating T cell and neutrophil functions. *J. Immunol.* 193:3549–3558. https://doi.org/10.4049/jimmunol.1401138

Jin, W., H.X. Xu, S.R. Zhang, H. Li, W.Q. Wang, H.L. Gao, C.T. Wu, J.Z. Xu, Z.H. Qi, S. Li, et al. 2019. Tumor-infiltrating NETs predict postsurgical survival in patients with pancreatic ductal adenocarcinoma. *Ann. Surg. Oncol.* 26:635–643. https://doi.org/10.1245/s10434-018-6941-4

Joshi, M.B., A. Lad, A.S. Bharath Prasad, A. Balakrishnan, L. Ramachandra, and K. Satyamoorthy. 2013. High glucose modulates IL-6 mediated immune homeostasis through impeding neutrophil extracellular trap formation. *FEBS Lett.* 587:2241–2246. https://doi.org/10.1016/j.febslet.2013.05.053

Klein, M., M.C. Brouwer, B. Angele, M. Geldhoff, G. Marquez, R. Varona, G. Häcker, H. Schmetzer, H. Häcker, S. Hammerschmidt, et al. 2014. Leukocyte attraction by CCL20 and its receptor CCR6 in humans and mice with pneumococcal meningitis. *PLoS One.* 9. e93057. https://doi.org/10.1371/journal.pone.0093057

Klok, F.A., M.J.H.A. Kruip, N.J.M. van der Meer, M.S. Arbous, D. Gommers, K.M. Kant, F.H.J. Kaptein, J. van Paassen, M.A.M. Stals, M.V. Huisman, and H. Endeman. 2020a. Confirmation of the high cumulative incidence of thrombotic complications in critically ill ICU patients with COVID-19: An updated analysis. *Thromb. Res.* 191:148–150. https://doi.org/10.1016/j.thromres.2020.04.041

Klok, F.A., M.J.H.A. Kruip, N.J.M. van der Meer, M.S. Arbous, D.A.M.P.J. Gommers, K.M. Kant, F.H.J. Kaptein, J. van Paassen, M.A.M. Stals, M.V. Huisman, and H. Endeman. 2020b. Incidence of thrombotic complications in critically ill ICU patients with COVID-19. *Thromb. Res.* 191:145–147. https://doi.org/10.1016/j.thromres.2020.04.013

Lánczky, A., Á. Nagy, G. Bottai, G. Munkácsy, A. Szabó, L. Santarpia, and B. Győrffy. 2016. miRpower: a web-tool to validate survival-associated miRNAs utilizing expression data from 2178 breast cancer patients. *Breast Cancer Res. Treat.* 160:439–446. https://doi.org/10.1007/s10549-016-4013-7

Langley, R.G., B.E. Elewski, M. Lebwohl, K. Reich, C.E. Griffiths, K. Papp, L. Puig, H. Nakagawa, L. Spelman, B. Sigurgeirsson, et al; FIXTURE Study Group. 2014. Secukinumab in plaque psoriasis--results of two phase 3 trials. *N. Engl. J. Med.* 371:326–338. https://doi.org/10.1056/NEJMoa1314258

Le, D.T., J.N. Uram, H. Wang, B.R. Bartlett, H. Kemberling, A.D. Eyring, A.D. Skora, B.S. Luber, N.S. Azad, D. Laheru, et al. 2015. PD-1 blockade in tumors with mismatch-repair deficiency. *N. Engl. J. Med.* 372:2509–2520. https://doi.org/10.1056/NEJMoa1500596

Lebwohl, M., B. Strober, A. Menter, K. Gordon, J. Weglowska, L. Puig, K. Papp, L. Spelman, D. Toth, F. Kerdel, et al. 2015. Phase 3 studies comparing brodalumab with ustekinumab in psoriasis. *N. Engl. J. Med.* 373:1318–1328. https://doi.org/10.1056/NEJMoa1503824

Lee, P.Y., Y. Kumagai, Y. Xu, Y. Li, T. Barker, C. Liu, E.S. Sobel, O. Takeuchi, S. Akira, M. Satoh, et al. 2011. IL-1α modulates neutrophil recruitment in chronic inflammation induced by hydrocarbon oil. *J. Immunol.* 186:1747–1754. https://doi.org/10.4049/jimmunol.1001328

Leppkes, M., C. Maueröder, S. Hirth, S. Nowecki, C. Günther, U. Billmeier, S. Paulus, M. Biermann, L.E. Munoz, M. Hoffmann, et al. 2016. Externalized decondensed neutrophil chromatin occludes pancreatic ducts and drives pancreatitis. *Nat. Commun.* 7:10973. https://doi.org/10.1038/ncomms10973

Li, H., D. Feng, Y. Cai, Y. Liu, M. Xu, X. Xiang, Z. Zhou, Q. Xia, M.J. Kaplan, X. Kong, et al. 2018. Hepatocytes and neutrophils cooperatively suppress bacterial infection by differentially regulating lipocalin-2 and neutrophil extracellular traps. *Hepatology.* 68:1604–1620. https://doi.org/10.1002/hep.29919

Lin, M., E. Carlson, E. Diaconu, and E. Pearlman. 2007. CXCL1/KC and CXCL5/LIX are selectively produced by corneal fibroblasts and mediate neutrophil infiltration to the corneal stroma in LPS keratitis. *J. Leukoc. Biol.* 81:786–792. https://doi.org/10.1189/jlb.0806502

Liu, C., S. Oveissi, R. Downs, J. Kirby, C. Nedeva, H. Puthalakath, P. Faou, M. Duan, and W. Chen. 2019. Semiquantitative proteomics enables mapping of murine neutrophil dynamics following lethal influenza virus infection. *J. Immunol.* 203:1064–1075. https://doi.org/10.4049/jimmunol.1900337

Long, G.V., J.S. Weber, J. Larkin, V. Atkinson, J.J. Grob, D. Schadendorf, R. Dummer, C. Robert, I. Márquez-Rodas, C. McNeil, et al. 2017. Nivolumab for patients with advanced melanoma treated beyond progression: analysis of 2 phase 3 clinical trials. *JAMA Oncol.* 3:1511–1519. https://doi.org/10.1001/jamaoncol.2017.1588

Lutz, E.R., H. Kinkead, E.M. Jaffee, and L. Zheng. 2014. Priming the pancreatic cancer tumor microenvironment for checkpoint-inhibitor immunotherapy. *OncoImmunology.* 3. e962401. https://doi.org/10.4161/21624011.2014.962401

Magro, C., J.J. Mulvey, D. Berlin, G. Nuovo, S. Salvatore, J. Harp, A. Baxter-Stoltzfus, and J. Laurence. 2020. Complement associated microvascular injury and thrombosis in the pathogenesis of severe COVID-19 infection: A report of five cases. *Transl. Res.* 220:1–13. https://doi.org/10.1016/j.trsl.2020.04.007

Makhezer, N., M. Ben Khemis, D. Liu, Y. Khichane, V. Marzaioli, A. Tlili, M. Mojallali, C. Pintard, P. Letteron, M. Hurtado-Nedelec, et al. 2019. NOX1-derived ROS drive the expression of Lipocalin-2 in colonic epithelial cells in inflammatory conditions. *Mucosal Immunol.* 12:117–131. https://doi.org/10.1038/s41385-018-0086-4

McAllister, F., and S.D. Leach. 2014. Targeting IL-17 for pancreatic cancer prevention. *Oncotarget.* 5:9530–9531. https://doi.org/10.18632/oncotarget.2618

McAllister, F., J.M. Bailey, J. Alsina, C.J. Nirschl, R. Sharma, H. Fan, Y. Rattigan, J.C. Roeser, R.H. Lankapalli, H. Zhang, et al. 2014. Oncogenic Kras activates a hematopoietic-to-epithelial IL-17 signaling axis in preinvasive pancreatic neoplasia. *Cancer Cell.* 25:621–637. https://doi.org/10.1016/j.ccr.2014.03.014

Murthy, P., A.D. Singhi, M.A. Ross, P. Loughran, P. Paragomi, G.I. Papachristou, D.C. Whitcomb, A.H. Zureikat, M.T. Lotze, H.J. Zeh Iii, et al. 2019. Enhanced neutrophil extracellular trap formation in acute pancreatitis contributes to disease severity and is reduced by chloroquine. *Front. Immunol.* 10:28. https://doi.org/10.3389/fimmu.2019.00028

Neeli, I., N. Dwivedi, S. Khan, and M. Radic. 2009. Regulation of extracellular chromatin release from neutrophils. *J. Innate Immun.* 1:194–201. https://doi.org/10.1159/000206974

Nograles, K.E., L.C. Zaba, E. Guttman-Yassky, J. Fuentes-Duculan, M. Suárez-Fariñas, I. Cardinale, A. Khatcherian, J. Gonzalez, K.C. Pierson, T.R. White, et al. 2008. Th17 cytokines interleukin (IL)-17 and IL-22 modulate distinct inflammatory and keratinocyte-response pathways. *Br. J. Dermatol.* 159:1092–1102.

Nywening, T.M., B.A. Belt, D.R. Cullinan, R.Z. Panni, B.J. Han, D.E. Sanford, R.C. Jacobs, J. Ye, A.A. Patel, W.E. Gillanders, et al. 2018. Targeting both tumour-associated CXCR2⁺ neutrophils and CCR2⁺ macrophages disrupts myeloid recruitment and improves chemotherapeutic responses in pancreatic ductal adenocarcinoma. *Gut.* 67:1112–1123. https://doi.org/10.1136/gutjnl-2017-313738

Okubo, K., M. Kamiya, Y. Urano, H. Nishi, J.M. Herter, T. Mayadas, D. Hirohama, K. Suzuki, H. Kawakami, M. Tanaka, et al. 2016. Lactoferrin suppresses neutrophil extracellular traps release in inflammation. *EBioMedicine.* 10:204–215. https://doi.org/10.1016/j.ebiom.2016.07.012

Pariser, D., E. Frankel, J. Schlessinger, Y. Poulin, R. Vender, R.G. Langley, X. Meng, A. Guana, and J. Nyirady. 2018. Efficacy of secukinumab in the treatment of moderate to severe plaque psoriasis in the North American subgroup of patients: pooled analysis of four phase 3 studies. *Dermatol. Ther. (Heidelb.).* 8:17–32. https://doi.org/10.1007/s13555-017-0211-4

Park, J., R.W. Wysocki, Z. Amoozgar, L. Maiorino, M.R. Fein, J. Jorns, A.F. Schott, Y. Kinugasa-Katayama, Y. Lee, N.H. Won, et al. 2016. Cancer cells induce metastasis-supporting neutrophil extracellular DNA traps. *Sci. Transl. Med*. 8. 361ra138. https://doi.org/10.1126/scitranslmed.aag1711

Patnaik, A., S.P. Kang, D. Rasco, K.P. Papadopoulos, J. Elassaiss-Schaap, M. Beeram, R. Drengler, C. Chen, L. Smith, G. Espino, et al. 2015. Phase I study of pembrolizumab (MK-3475; anti-PD-1 monoclonal antibody) in patients with advanced solid tumors. *Clin. Cancer Res*. 21:4286–4293. https://doi.org/10.1158/1078-0432.CCR-14-2607

Provenzano, P.P., C. Cuevas, A.E. Chang, V.K. Goel, D.D. Von Hoff, and S.R. Hingorani. 2012. Enzymatic targeting of the stroma ablates physical barriers to treatment of pancreatic ductal adenocarcinoma. *Cancer Cell*. 21:418–429. https://doi.org/10.1016/j.ccr.2012.01.007

Pushalkar, S., M. Hundeyin, D. Daley, C.P. Zambirinis, E. Kurz, A. Mishra, N. Mohan, B. Aykut, M. Usyk, L.E. Torres, et al. 2018. The pancreatic cancer microbiome promotes oncogenesis by induction of innate and adaptive immune suppression. *Cancer Discov*. 8:403–416. https://doi.org/10.1158/2159-8290.CD-17-1134

Rada, B., and T.L. Leto. 2008. Oxidative innate immune defenses by Nox/Duox family NADPH oxidases. *Contrib. Microbiol*. 15:164–187. https://doi.org/10.1159/000136357

Rayes, R.F., J.G. Mouhanna, I. Nicolau, F. Bourdeau, B. Giannias, S. Rousseau, D. Quail, L. Walsh, V. Sangwan, N. Bertos, et al. 2019. Primary tumors induce neutrophil extracellular traps with targetable metastasis promoting effects. *JCI Insight*. 5. 128008. https://doi.org/10.1172/jci.insight.128008

Reich, K., A. Blauvelt, A. Armstrong, R.G. Langley, T. Fox, J. Huang, C. Papavassilis, E. Liang, P. Lloyd, and G. Bruin. 2017. Secukinumab, a fully human anti-interleukin-17A monoclonal antibody, exhibits minimal immunogenicity in patients with moderate-to-severe plaque psoriasis. *Br. J. Dermatol*. 176:752–758. https://doi.org/10.1111/bjd.14965

Riquelme, E., A. Maitra, and F. McAllister. 2018. Immunotherapy for pancreatic cancer: more than just a gut feeling. *Cancer Discov*. 8:386–388. https://doi.org/10.1158/2159-8290.CD-18-0123

Riquelme, E., Y. Zhang, L. Zhang, M. Montiel, M. Zoltan, W. Dong, P. Quesada, I. Sahin, V. Chandra, A. San Lucas, et al. 2019. Tumor microbiome diversity and composition influence pancreatic cancer outcomes. *Cell*. 178:795–806.e12. https://doi.org/10.1016/j.cell.2019.07.008

Rouault, C., V. Pellegrinelli, R. Schilch, A. Cotillard, C. Poitou, J. Tordjman, H. Sell, K. Clément, and D. Lacasa. 2013. Roles of chemokine ligand-2 (CXCL2) and neutrophils in influencing endothelial cell function and inflammation of human adipose tissue. *Endocrinology*. 154:1069–1079. https://doi.org/10.1210/en.2012-1415

Royal, R.E., C. Levy, K. Turner, A. Mathur, M. Hughes, U.S. Kammula, R.M. Sherry, S.L. Topalian, J.C. Yang, I. Lowy, et al. 2010. Phase 2 trial of single agent Ipilimumab (anti-CTLA-4) for locally advanced or metastatic pancreatic adenocarcinoma. *J. Immunother*. 33:828–833. https://doi.org/10.1097/CJI.0b013e3181eec14c

Strober, B.E., R.G.B. Langley, A. Menter, M. Magid, B. Porter, T. Fox, J. Safi, Jr., and C. Papavassilis. 2018. No elevated risk for depression, anxiety or suicidality with secukinumab in a pooled analysis of data from 10 clinical studies in moderate-to-severe plaque psoriasis. *Br. J. Dermatol*. 178:e105–e107. https://doi.org/10.1111/bjd.16051

Tillack, K., P. Breiden, R. Martin, and M. Sospedra. 2012. T lymphocyte priming by neutrophil extracellular traps links innate and adaptive immune responses. *J. Immunol*. 188:3150–3159. https://doi.org/10.4049/jimmunol.1103414

Toussaint, M., D.J. Jackson, D. Swieboda, A. Guedán, T.D. Tsourouktsoglou, Y.M. Ching, C. Radermecker, H. Makrinioti, J. Aniscenko, N.W. Bartlett, et al. 2017. Host DNA released by NETosis promotes rhinovirus-induced type-2 allergic asthma exacerbation. *Nat. Med*. 23:681–691. https://doi.org/10.1038/nm.4332

Uriarte, S.M., D.W. Powell, G.C. Luerman, M.L. Merchant, T.D. Cummins, N.R. Jog, R.A. Ward, and K.R. McLeish. 2008. Comparison of proteins expressed on secretory vesicle membranes and plasma membranes of human neutrophils. *J. Immunol*. 180:5575–5581. https://doi.org/10.4049/jimmunol.180.8.5575

Wang, Y., M. Li, S. Stadler, S. Correll, P. Li, D. Wang, R. Hayama, L. Leonelli, H. Han, S.A. Grigoryev, et al. 2009. Histone hypercitrullination mediates chromatin decondensation and neutrophil extracellular trap formation. *J. Cell Biol*. 184:205–213. https://doi.org/10.1083/jcb.200806072

Winograd, R., K.T. Byrne, R.A. Evans, P.M. Odorizzi, A.R. Meyer, D.L. Bajor, C. Clendenin, B.Z. Stanger, E.E. Furth, E.J. Wherry, et al. 2015. Induction of T-cell immunity overcomes complete resistance to PD-1 and CTLA-4 blockade and improves survival in pancreatic carcinoma. *Cancer Immunol. Res*. 3:399–411. https://doi.org/10.1158/2326-6066.CIR-14-0215

Wolchok, J.D., V. Chiarion-Sileni, R. Gonzalez, P. Rutkowski, J.J. Grob, C.L. Cowey, C.D. Lao, J. Wagstaff, D. Schadendorf, P.F. Ferrucci, et al. 2017. Overall survival with combined nivolumab and ipilimumab in advanced melanoma. *N. Engl. J. Med*. 377:1345–1356. https://doi.org/10.1056/NEJMoa1709684

Xu, Z., L. Shi, Y. Wang, J. Zhang, L. Huang, C. Zhang, S. Liu, P. Zhao, H. Liu, L. Zhu, et al. 2020. Pathological findings of COVID-19 associated with acute respiratory distress syndrome. *Lancet Respir. Med*. 8:420–422. https://doi.org/10.1016/S2213-2600(20)30076-X

Zhang, Y., A. Velez-Delgado, E. Mathew, D. Li, F.M. Mendez, K. Flannagan, A.D. Rhim, D.M. Simeone, G.L. Beatty, and M. Pasca di Magliano. 2017. Myeloid cells are required for PD-1/PD-L1 checkpoint activation and the establishment of an immunosuppressive environment in pancreatic cancer. *Gut*. 66:124–136. https://doi.org/10.1136/gutjnl-2016-312078

Zhang, Y., M. Zoltan, E. Riquelme, H. Xu, I. Sahin, S. Castro-Pando, M.F. Montiel, K. Chang, Z. Jiang, J. Ling, et al. 2018. Immune cell production of interleukin 17 induces stem cell features of pancreatic intraepithelial neoplasia cells. *Gastroenterology*. 155:210–223.e3. https://doi.org/10.1053/j.gastro.2018.03.041

Zhu, Y., B.L. Knolhoff, M.A. Meyer, T.M. Nywening, B.L. West, J. Luo, A. Wang-Gillam, S.P. Goedegebuure, D.C. Linehan, and D.G. DeNardo. 2014. CSF1/CSF1R blockade reprograms tumor-infiltrating macrophages and improves response to T-cell checkpoint immunotherapy in pancreatic cancer models. *Cancer Res*. 74:5057–5069. https://doi.org/10.1158/0008-5472.CAN-13-3723

Zuo, Y., S. Yalavarthi, H. Shi, K. Gockman, M. Zuo, J.A. Madison, C. Blair, A. Weber, B.J. Barnes, M. Egeblad, et al. 2020. Neutrophil extracellular traps in COVID-19. *JCI Insight*. 5. 138999.
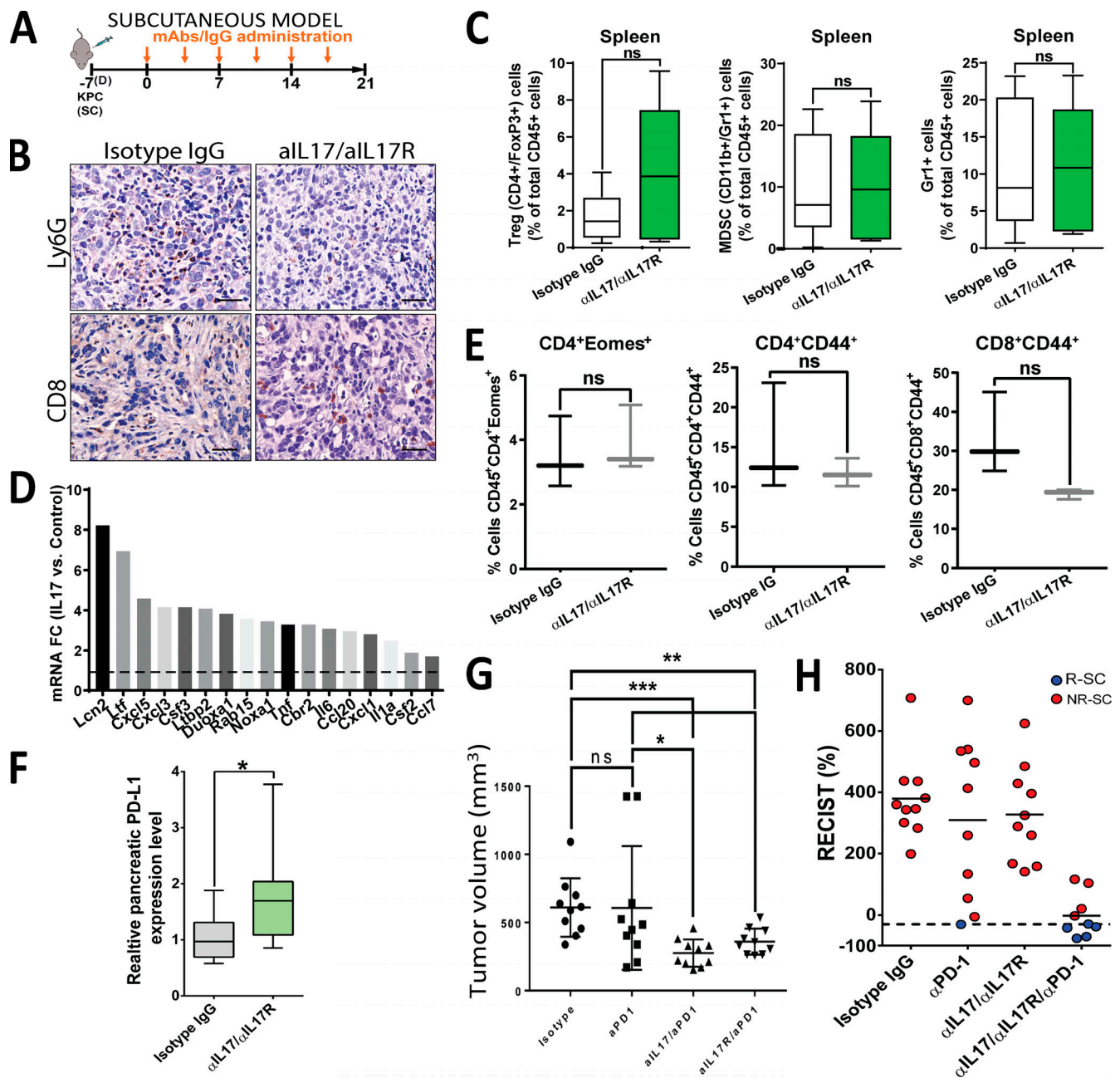
Figure S1. **Immunological effects of IL17 blockade and antitumoral effects of combination with PD-1 blockade in subcutaneous tumors. (A)** Experimental protocol for subcutaneous implantation of KPC cells into syngeneic mice. Cells were treated with isotype IgG, aPD-1, aIL17/aIL17R, or aIL17/aIL17R/aPD-1 antibodies. **(B)** Representative IHC staining for Ly6G and CD8+ cells in tumors from A. Scale bars represent 100 μm. **(C)** Flow cytometric analysis showing CD45+/CD4+/FoxP3+ (left), CD45+/CD11b+/Gr1+ (middle), and CD45+/Gr1+ (right) cells in spleens from mice implanted with orthotopic KPC tumors. **(D)** mRNA upregulation fold change (FC) of neutrophil-related genes in KPC cells upregulated by ≥1.5-fold after in vitro stimulation with IL17 for 7 d, as identified by RNA sequencing. All genes were statistically significantly upregulated. **(E)** Exhaustion markers CD4+/Eomes+ (left), CD4+CD44+ (middle), and CD8+/CD44+ (right) detected by flow cytometry on orthotopic tumors. **(F)** Quantitative RT-PCR analysis of PD-L1 gene relative expression in orthotopic tumors (n = 10 mice/group). **(G)** Subcutaneous tumor volumes at endpoint in A. **(H)** RECIST analysis of subcutaneously implanted KPC tumors from A. R, responders; NR, nonresponders. *, P < 0.05; **, P < 0.01; ***, P < 0.001.
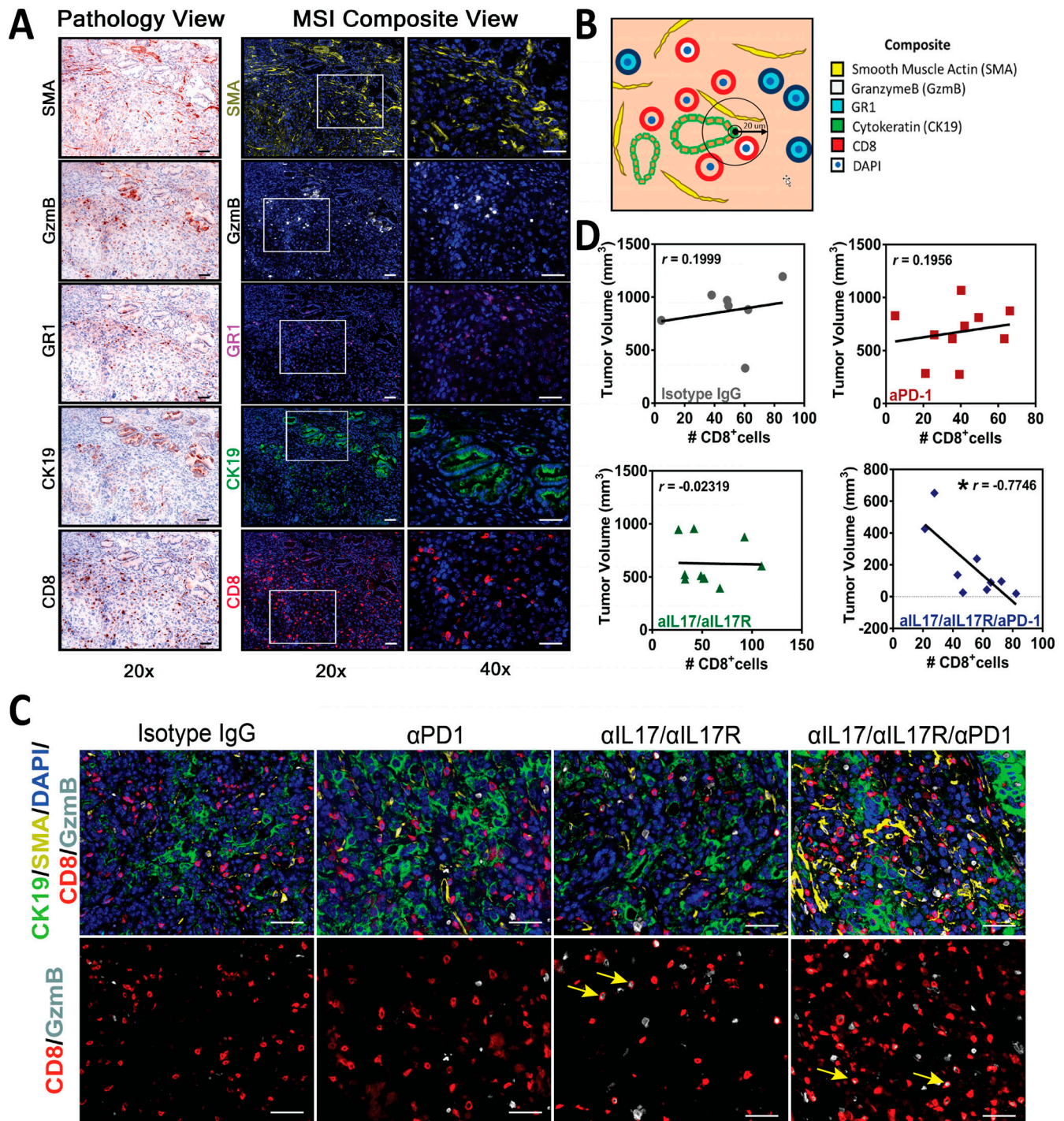
Figure S2. **Multiplex immunofluorescence characterization of pancreatic tumor microenvironment. (A)** Multiplex staining. Pathology view and multispectral image (MSIs) composite view for individual markers at 20× and 40× magnification. Scale bars represent 50 µm. **(B)** Diagram for visualization of spatial quantification. In this example, the number of CD8+/GzmB+ cells within 20-µm radius from CK19+ cells is quantified. **(C)** Representative pictures of multiplex IF staining showing CD8, GzmB, CK19, SMA, and DAPI (top panels) staining in orthotopic tumor tissues from Fig. 4 B. Bottom panels show only CD8/GzmB. Scale bars represent 50 µm. Yellow arrows indicate double-positive cells for CD8 and GzmB staining. **(D)** Correlation analysis between tumor volume and CD8+ T cell frequency in the four treatment arms in C.
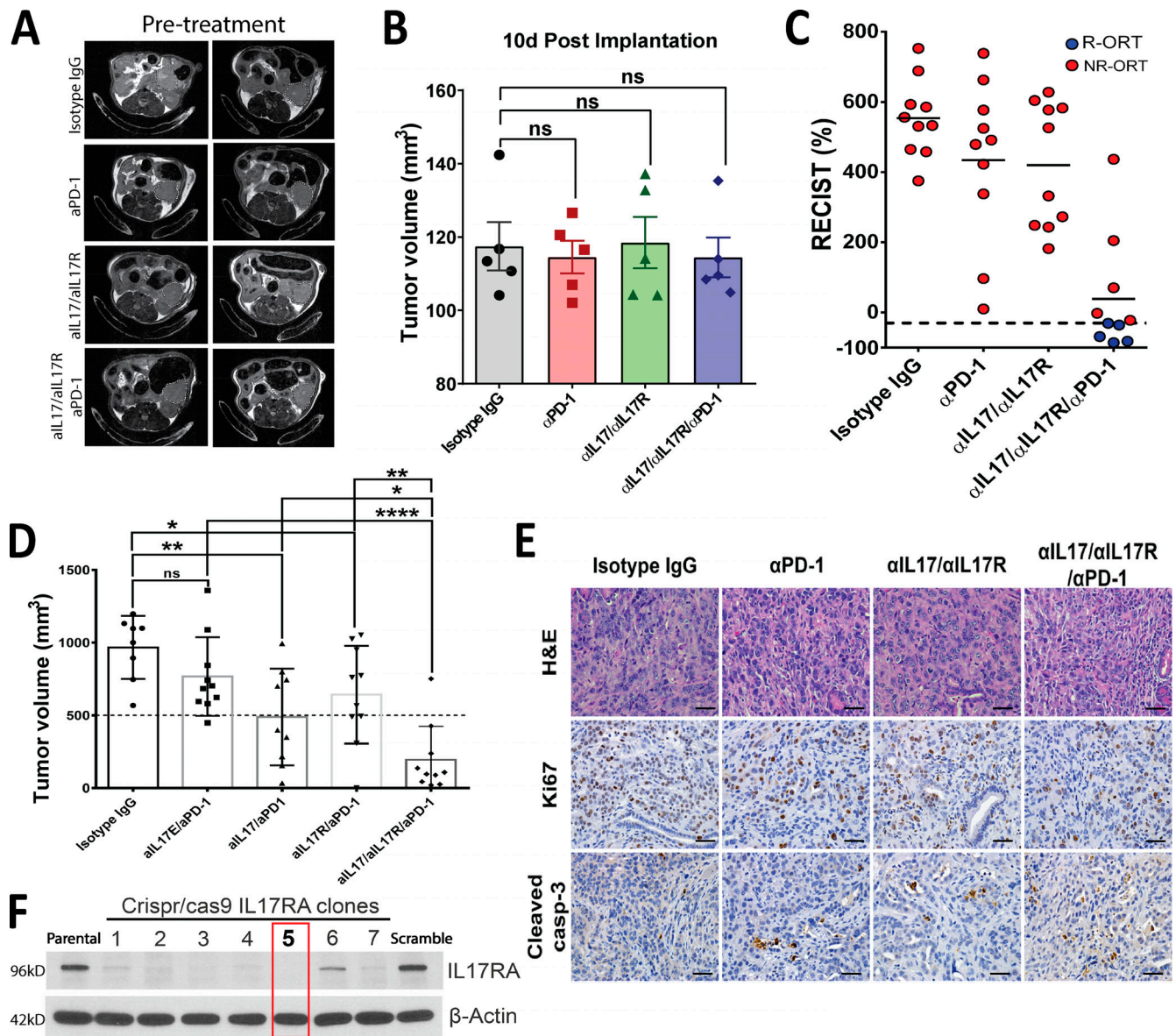
Figure S3. **Antitumoral effect of combination of IL17 and PD-1 blockade in orthotopic tumors. (A)** Axial abdominal MRI scans of mice in all groups before the start of treatment at 10 d after orthotopic tumor implantation. **(B)** Quantification of tumor volumes as measured by MRI in A. **(C)** RECIST analysis in mice with orthotopically implanted KPC tumors in Fig. 4 B. R, responders; NR, nonresponders. **(D)** Tumor volumes of KPC tumors orthotopically implanted into syngeneic hosts and treated with isotype, aIL17E/aPD-1, aIL17/aPD-1, aIL17RA/aPD-1, and aIL17R/aIL17R/aPD-1. **(E)** Representative pictures of H&E and IHC staining for Ki67 and cleaved caspase 3 on tumor tissues from KPC cells orthotopically implanted in Fig. 4 B. Scale bars represent 100 μm. **(F)** Immunoblotting for IL17RA on CRISPR/Cas9 IL17RA-KO KPC cell clones. β-actin was used as a loading control. Parental KPC cells and scramble negative control cells are also included. *, P < 0.05; **, P < 0.01; ****, P < 0.0001.
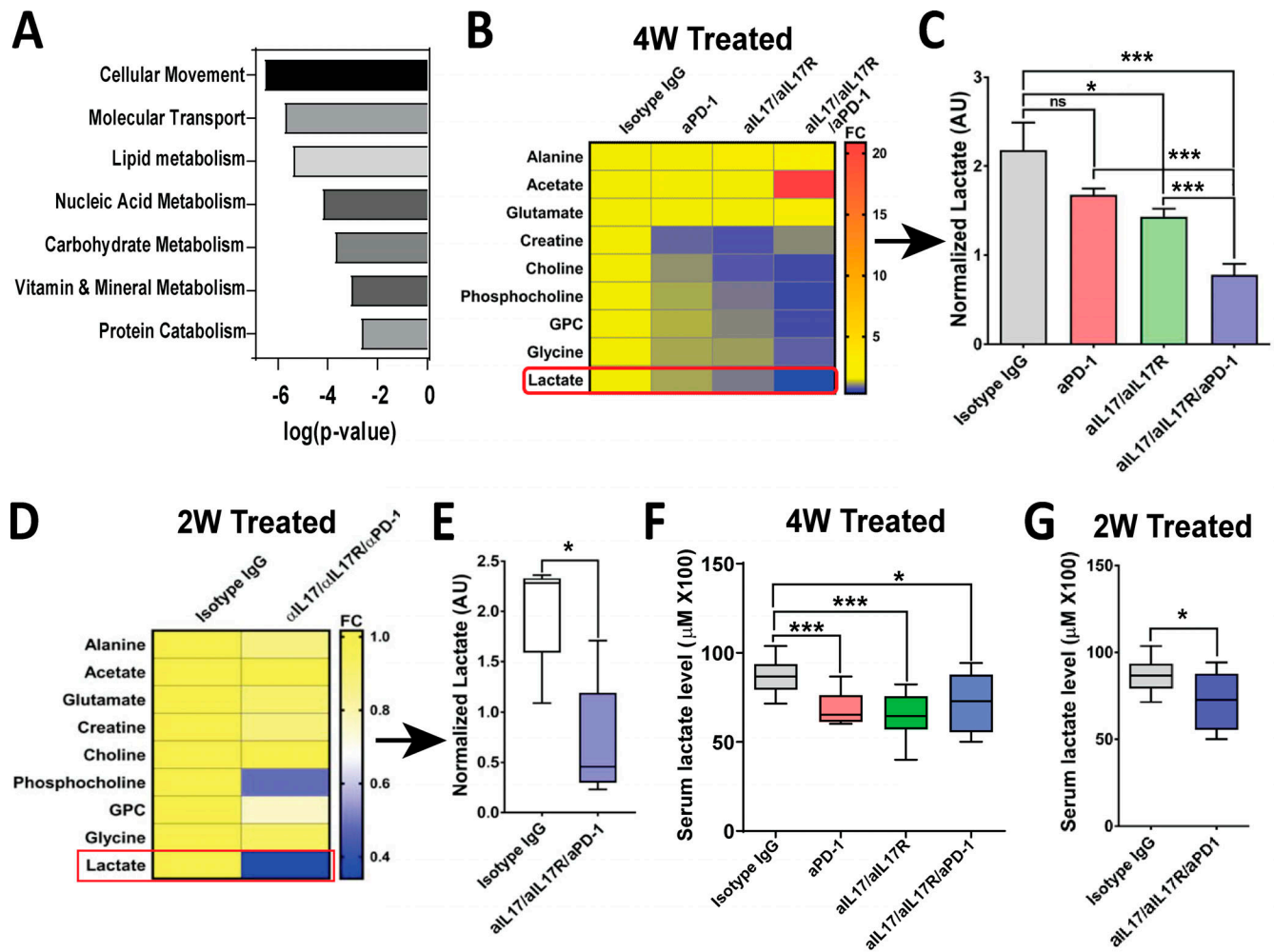
Figure S4. **Tumor metabolic changes with combination of IL17 and PD-1 blockade. (A)** Ingenuity Pathway Analysis (IPA) showing top molecular and cellular functions predicted using genes significantly regulated in murine orthotopic KPC tumors treated with neutralizing aIL17/aIL17R/aPD-1 antibodies versus isotype IgG control ($n = 10$). X axis indicates biological functions with P < 0.05. **(B)** Heat map representing normalized metabolites in murine orthotopic KPC tumors treated with isotype IgG, aPD-1, aIL17/aIL17R, and aIL17/aIL17R/aPD-1 antibodies for 4 wk ($n = 10$). GPC, glycerophosphocholine. **(C)** Quantification of normalized lactate levels measured by NMR spectroscopy in B. **(D)** Heat map representing normalized metabolites in murine orthotopic KPC tumors treated with isotype IgG and aIL17/aIL17R/aPD-1 antibodies for 2 wk ($n = 10$). **(E)** Quantification of normalized lactate levels measured by NMR spectroscopy in D. **(F)** Serum lactate levels in mice from B. **(G)** Serum lactate levels in mice from D. *, P < 0.05; ***, P < 0.001.
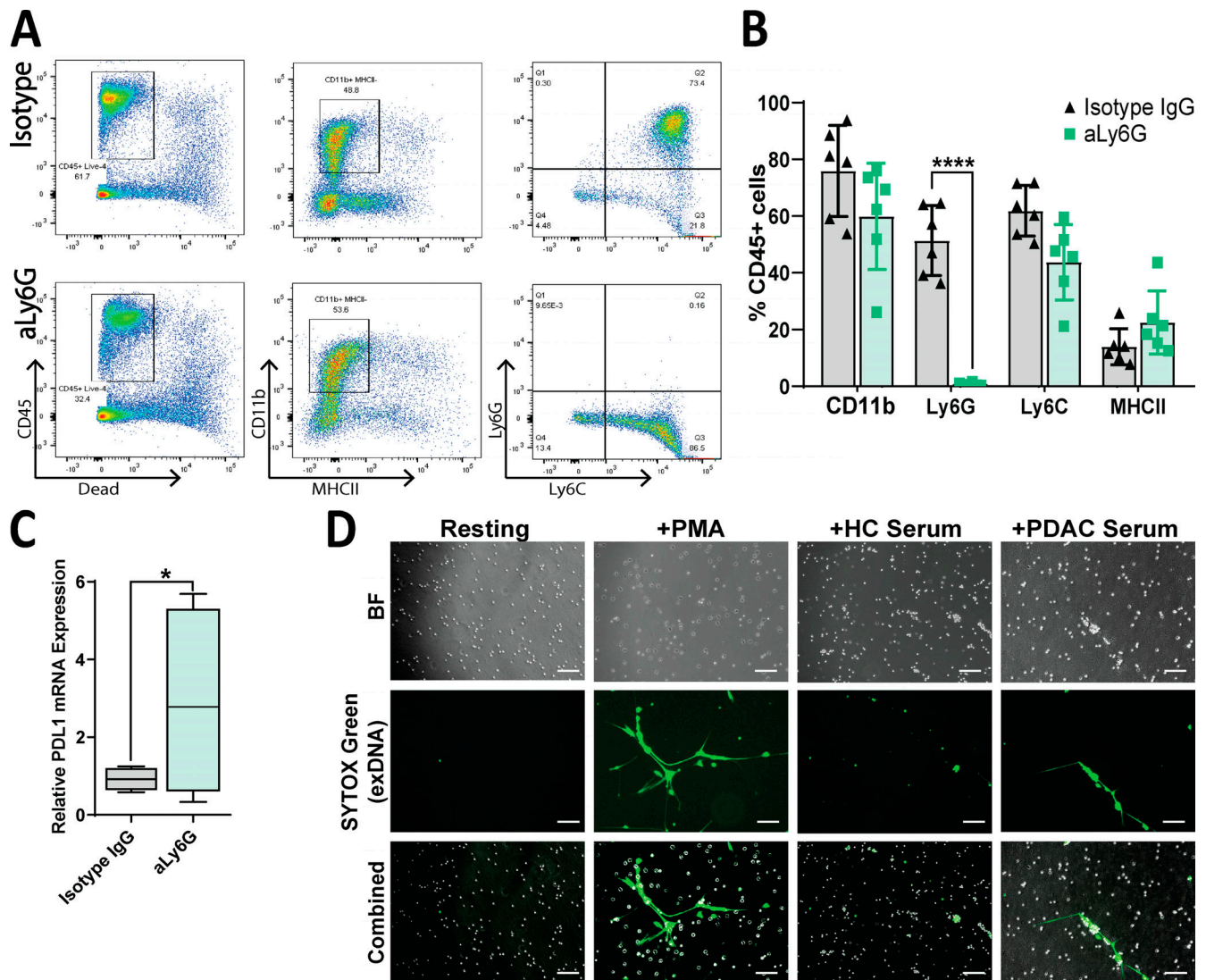
Figure S5. **Neutrophil depletion and NETosis imaging with human samples. (A)** Representative plots depicting flow cytometric analysis of orthotopic tumors treated with isotype IgG or aLy6G antibodies. **(B)** Quantification of indicated markers as gated in A, as a percentage of viable CD45+ cells. **(C)** Quantitative RT-PCR analysis of relative PD-L1 mRNA expression in orthotopic tumors treated with isotype IgG or aLy6G antibodies (n = 5 per group). **(D)** Representative images of human neutrophils stimulated with PMA or serum of healthy control subjects (HC) or patients with PDAC. Green = extracellular (ex) DNA, as stained by SYTOX Green. Scale bars represent 100 μm. *, $P < 0.05$; ****, $P < 0.0001$. BF, bright field.

Tables S1–S3 are provided online as separate Word documents. Table S1 shows RNA sequencing of tumors from mice treated with isotype IgG versus aIL17/IL17R mAb. Table S2 shows RNA sequencing of tumors from mice treated with isotype IgG versus aIL17/ IL17R + anti-PD-1 blockade. Table S3 provides reagent information.